An Analog Front End for the Coherent All-Sky Monitor

Thesis by
Michael Gutierrez

In Partial Fulfillment of the Requirements for the
Degree of
B.S., Astrophysics

CALIFORNIA INSTITUTE OF TECHNOLOGY
Pasadena, California

2025
Defended 8 June 2025

Michael Gutierrez
ORCID: xxxxx

ACKNOWLEDGEMENTS

Thanks to the Class of 1970 Memorial SURF Fund for sponsoring the SURF project during Summer 2024 which this thesis grew out of, and to the Moffett fund for the means to bring it into physical reality.

To all my mentors throughout this process — Vikram Ravi, Liam Connor, Sandy Weinreb, Nivedita Mahesh, Jonas Flygare, Mark Hodges, David Hodge, Kiran Shila, Saren Daghlian, Calvin Leung, and Keith Bannister — I feel so lucky to have had the opportunity to work with you and learn from you! It has been the highlight of my Caltech experience.

ABSTRACT

The study of astronomical transients is often limited by a fundamental trade-off between a telescope's sensitivity and its field of view. To detect the faint, rare, and unpredictable phenomena that hold the keys to astrophysical mysteries like the origin of Fast Radio Bursts (FRBs), an instrument with both enormous collecting area and a vast field of view is required. The Coherent All-Sky Monitor (CASM) project addresses this challenge by pioneering a large-N, small-D aperture array of 256 dual-polarization antennas at Owens Valley Radio Observatory. This thesis details the design, simulation, fabrication, and testing of the analog front end for CASM-256, the core component enabling its scientific mission. I present the evolution of the antenna design, beginning with a prototype (CASM-6) based on the Long Wavelength Array (LWA) bent-dipole concept and culminating in a scalable, low-cost printed dipole array (CASM-256) inspired by the ARTE experiment. Through extensive electromagnetic simulation using ANSYS HFSS, the final antenna was optimized to meet the stringent requirements for a low system temperature ($\lesssim$ 50 K) and a wide bandwidth (S_{11} < -10 dB) across the 375-500 MHz band, all while achieving the requisite 10,000 deg^2 field of view. Physical prototypes of the final design were fabricated and tested, showing excellent agreement with simulations. This work provides a robust and cost-effective antenna solution, paving the way for the full deployment of CASM-256 and its quest to uncover a local-Universe sample of FRBs, discover novel Galactic transients, and search for electromagnetic counterparts to gravitational wave events.

TABLE OF CONTENTS

NOMENCLATURE

T_{rec}**.** Receiver Temperature.

T_{sys}**.** System Temperature.

Beam width. The full angle of an antenna's Field of View. Also called Full Width at Half-Maximum (FWHM). Roughly $\sqrt{\Omega_{\text{FoV}}}$.

CASM. Coherent All-Sky Monitor.

CGM. Circumgalactic Medium.

Coax. Coaxial cable.

Crosstalk. Unwanted leakage of signals.

Element (of a dipole antenna). A discrete conducting object acting as one of the poles in the dipole antenna, usually one quarter wavelength.

ESD. Electrostatic Discharge.

FoV. Field of View.

FPGA. Field Programmable Gate Array; a versatile type of integrated circuit which is designed to be reprogrammable to suit different purposes, notably high-performance computing (HPC).

FRB. Fast Radio Burst.

IGM. Intergalactic Medium.

LNA. Low Noise Amplifier.

Mutual coupling. Leakage of signal received by one antenna in an array into adjacent antennas.

OVRO. Owens Valley Radio Observatory.

PCB. Printed Circuit Board.

Radome. Radar dome, a structural, weatherproof enclosure that protects an antenna.

RFI. Radio Frequency Interference.

S-parameters. Of an RF network, S_{xy} is the S-parameter quantifying the amount (and phase) of a signal put into port x that comes out of port y. Usually we look at the $\log_{10}$ of the magnitude of S-parameters in dB. An antenna is a one-port network, and S_{11} quantifies how much of an incoming signal is reflected back from the antenna. A good antenna will accept most of the incoming signal and not reflect much back; the typical benchmark is -10 dB, meaning an antenna is "good" at a given frequency if less than 1/10 of an incident signal of that frequency is reflected.

SEFD. System Equivalent Flux Density.

SNR. Signal-to-Noise Ratio.

VNA. Vector Network Analyzer.

Chapter 1

INTRODUCTION

1.1 Executive Summary

Many of the most interesting phenomena in astrophysics are exceedingly faint, rare, or both. The discovery power of a telescope is therefore dependent on both its sensitivity to small signals and its simultaneous field of view (FoV). For traditional telescopes, astronomers achieve high sensitivities by building massive mirrors or dishes to collect as much light as possible. However, focusing all of that light onto a single receiver creates a direct tradeoff between collecting area and FoV. For example, the FoV of the exquisitely sensitive 1000-ft Arecibo Telescope was less than one percent of a square degree – a mere 10^{-8} of the entire celestial sphere.

This limitation is particularly acute in low-frequency radio astronomy. The advent of powerful digital signal processing, driven by Moore's Law, has allowed us to rethink the traditional approach. Now, the "optics" of an interferometric array can be purely digital, performed on large compute clusters. Instead of one large dish, we can use a vast number of small antennas—a "large-N, small-D" array—and combine their outputs digitally to synthesize a large telescope. This paradigm, exemplified by instruments like the DSA-110 and the proposed DSA-2000 (Hallinan et al., 2019), allows us to retain a wide FoV while clawing back the sensitivity lost by having smaller individual elements.

The logical conclusion of this concept is the aperture array, where antenna elements are placed directly on the ground without any focusing dish at all. The Coherent All-Sky Monitor (CASM) is such an instrument. To be located at Owens Valley Radio Observatory (OVRO), CASM-256 will be an interferometric array of 256 dual-polarization antennas operating in the 375-500 MHz band. By forgoing dishes, an individual antenna can "see" half of the visible sky at once, granting CASM-256 an unprecedented instantaneous FoV of approximately 10,000 deg^2. By combining the signals from all 256 antennas, we can achieve the sensitivity needed to open a new window on the transient sky. This thesis focuses on the most critical component of this endeavor: the design of a low-cost, high-performance, and scalable antenna and analog front-end system that makes the entire project feasible.

1.2 Scientific Motivation

The biggest challenge for radio astronomy in the time domain is that our transient signals of interest are, for the most part, completely unpredictable. With the exception of a few known repeating sources, it is simply not efficient to point highly sensitive, narrow-field telescopes at random patches of the sky and hope to get lucky. To build a substantive sample of radio transient populations—unbiased by repetition timescale or sky location—we require an instrument that watches the entire sky, all the time.

CASM-256 will be the first experiment to simultaneously monitor half of the visible radio sky with millisecond resolution, exploring a completely new region of transient parameter space defined by fluence and duration. While instruments like the Canadian Hydrogen Intensity Mapping Experiment

(CHIME) and the Deep Synoptic Array (DSA-110) have been revolutionary for FRB science, their fields of view are orders of magnitude smaller than what an aperture array can achieve. As shown in Figure 1.1, CASM-256's 10,000 deg^2 FoV dwarfs that of CHIME ($\approx$ 200 deg^2) and DSA-110 ($\approx$ 10 deg^2). This capability is guaranteed to produce transformative science.

- **A Local Universe Sample of FRBs:** The origin of Fast Radio Bursts (FRBs) remains one of the great outstanding mysteries in astrophysics. While instruments like the DSA-110 have localized a significant number of FRBs, most are at high redshift ($z \gtrsim 0.3$), making detailed follow-up of their host galaxies and local environments exceedingly difficult (Sharma, 2024; Connor et al., 2024). We desperately need a local-Universe sample with which we can pin down their galactic environment and search for prompt multiwavelength emission. The only current example, the Galactic FRB from magnetar SGR 1935+2154, was only understood because of its proximity (Bochenek et al., 2020). CASM-256's immense FoV will enable the discovery of an unprecedented sample of these bright, nearby FRBs.

- **Galactic Radio Transients:** In the past few years, a new class of periodic radio sources with unusually long spin periods (minutes to hours) has been discovered. These objects, possibly ultra-slow magnetars or highly magnetized white dwarfs, are difficult to find in typical pulsar surveys. An all-sky monitor like CASM will have such objects in its field of view for hours at a time, making it an ideal discovery machine for this new population. Furthermore, CASM will be perfectly suited to detect rare, mega-Jansky bursts from Galactic magnetars, providing crucial data points linking them to the cosmological FRB population.

- **Prompt Emission from Gravitational Waves:** Merging compact objects, such as neutron stars, are predicted to produce fast, coherent radio emission at the moment of coalescence (Most and Philippov, 2022). To date, no radio telescope has been observing a gravitational wave event *at the time of the merger*. With its approximately 10,000 deg^2 FoV, CASM-256 will have approximately half of all Northern Hemisphere LIGO-Virgo-KAGRA events within its view, providing the first real opportunity to detect prompt or precursor radio emission and open a new chapter in multi-messenger astronomy.

- **A Measurement of the Milky Way's Circumgalactic Medium (CGM):** The dispersion of an FRB's signal is dominated by the intergalactic medium (IGM). For a nearby sample ($\lesssim$ 100 Mpc), however, the IGM contribution is minimal. The observed dispersion will instead be dominated by baryons in the host galaxy and our own Milky Way. A large sample of nearby FRBs from CASM will provide a powerful and unique probe of the baryonic content and structure of our own Galaxy's halo (Ravi et al., 2023).

- **Technology for the Future:** The antenna and analog systems developed in this thesis are designed for low-cost mass production. They serve as a critical pathfinder, creating and proving the novel technology required for future, even larger arrays on the scale of thousands of elements.

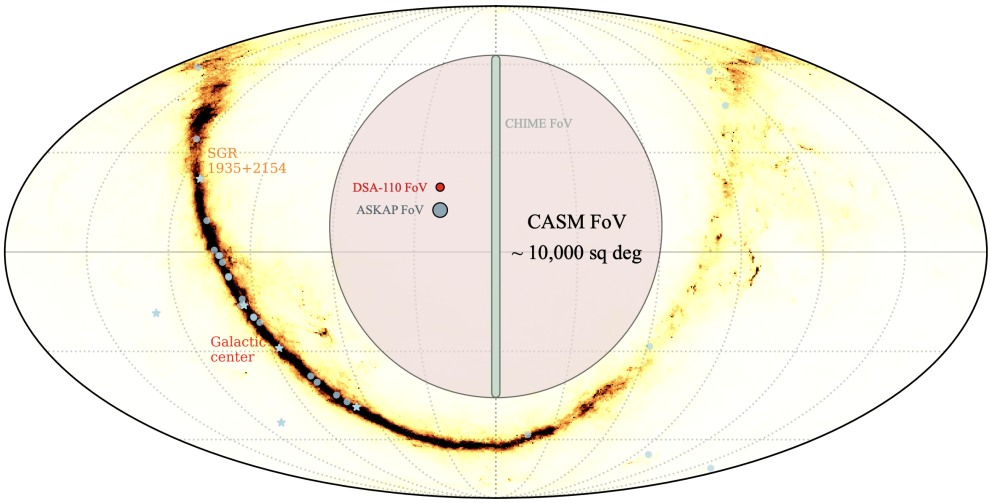

Figure 1.1: The large FoV of CASM-256 will find extreme, rare radio phenomena. The 10,000 deg^2 FoV of our proposed aperture array is visualized as a large mauve circle with comparisons to CHIME (green), DSA-110 (red), and ASKAP in Australia (blue). CASM will be fully stationary, meaning the sky will pass overhead, sometimes with significant numbers of Galactic magnetars in our beam (light blue circles) and sometimes with purely off-plane pointings, as shown. We plot these over the Planck HFI 857 GHz map, which is a proxy for molecular gas and therefore star-formation, which is why the magnetars reside in dark regions. Figure courtesy of Liam Connor.

Chapter 2

DESIGN CONSTRAINTS AND REQUIREMENTS

The design of the CASM-256 analog front end is guided by a series of top-down constraints derived from the primary science goals, and bottom-up constraints imposed by budget and the physical environment. The key design requirements are summarized in Table 2.1. In this chapter, we will derive these requirements and discuss their implications for the antenna design.

Quantity	Constraint
Cost per antenna	$\leq$ \$300
SEFD	$\lesssim$ 5 kJy
T_{sys}	$\leq$ 50 K
Antenna bandwidth ($S_{11} < -10$dB)	$\geq$ 125 MHz
Ω_{FoV} @ -3dB from max	$\approx 10,000$ deg^2 (π sr.)
Total gain of LNA	$\approx$ 30dB
Filter bandpass	$\leq$ 125 MHz
Time resolution (Δt)	1 ms

Table 2.1: A summary of the key design constraints for the CASM-256 analog front end.

2.1 Cost and Scalability

Since scalability is the defining feature of this array, the most important constraint on the design is cost (in fact, the “C" in CASM originally stood for “Cheap"). With a total hardware budget of approximately \$75,000 for 256 antennas, we must keep the price per antenna below \$300. This budget must cover the antenna itself, the low-noise amplifier (LNA), mounting hardware, and cabling. Furthermore, this cost constraint implicitly demands a design that minimizes labor. The antennas must require minimal assembly with as few unique parts as possible, favoring integrated designs like printed circuit board (PCB) antennas over those requiring manual assembly of many small components.

2.2 Performance Requirements

The performance of a radio telescope is fundamentally about achieving a sufficient signal-to-noise ratio (SNR) on a target of interest. For CASM-256, the primary targets are bright, nearby Fast Radio Bursts. The SNR for a transient source is given by:

$$\text{SNR} = \frac{S_{\text{FRB}}}{\text{SEFD}} \sqrt{2B\Delta t}$$

where S_{FRB} is the flux density of the burst, B is the observing bandwidth, Δt is the integration time, and SEFD is the System Equivalent Flux Density. The SEFD represents the flux density of a source that would double the system noise power, and is the key metric for array sensitivity:

$$\text{SEFD} = \frac{2k_B T_{\text{sys}}}{N_{\text{ant}} A_{\text{eff}}}$$

Here, k_B is the Boltzmann constant, T_{sys} is the system temperature, N_{ant} is the number of antennas, and A_{eff} is the effective collecting area of a single antenna.

To detect FRBs with flux densities $S_{\rm FRB} \geq 100$ Jy at a minimum SNR of 10, over our maximum bandwidth of 125 MHz and a time resolution of 1 ms, we can calculate the maximum allowable SEFD to be 5 kJy.

The effective area of a single dipole antenna is related to its field of view by the simple relation $A_{\rm eff}\,\Omega_{\rm FoV} \approx \lambda^2$. For an all-sky instrument, we require $\Omega_{\rm FoV} \approx \pi$ steradians (sr). At our central frequency of 437.5 MHz ($\lambda \approx 68$ cm), this gives a single antenna an effective area of $A_{\rm eff} \approx (0.68{\rm m})^2/\pi$ sr ≈ 0.15 m^2.

With $N_{\rm ant} = 256$ antennas and our calculated $A_{\rm eff}$, we can now solve for the most critical parameter for the front-end electronics: the system temperature, $T_{\rm sys}$. Plugging our values into the SEFD equation, we find that to achieve an SEFD of 5 kJy, the maximum acceptable system temperature is approximately 50 K. The system temperature is the sum of the sky temperature and the receiver temperature, $T_{\rm sys} = T_{\rm sky} + T_{\rm rec}$. In our observing band, the sky temperature $T_{\rm sky}$ is dominated by diffuse Galactic synchrotron emission and has an average value of about 25 K (Oliveira-Costa et al., 2008). This leaves only 25 K for the entire receiver chain, including the antenna and LNA. This stringent requirement drives much of the analog design, as any loss in the system before the first stage of amplification contributes directly to $T_{\rm rec}$.

2.3 Frequency Band and RFI Environment

Optimizing for Transient Detection

The choice of observing band is a critical trade-off, driven by the desire to maximize the detection rate of transient events. For a population of sources with a cumulative number count $N(>S) \propto S^{-\alpha}$, the detection rate scales as $Rate \propto \Omega_{\rm sky} \times S_{\rm min}^{-\alpha}$. For sources distributed uniformly in a Euclidean volume, as is expected for the nearby FRB population, the power-law index $\alpha = 3/2$ (Oppermann, Connor, and Pen, 2016). By substituting the expression for sensitivity $S_{\rm min}$ from the radiometer equation, we can derive how the event rate depends on key telescope parameters:

$$Rate \propto \Omega_{\rm sky} N_{\rm ant}^{3/2} B^{3/4}$$

This simple relation clearly demonstrates that to maximize our science return, we should prioritize increasing the field of view ($\Omega_{\rm sky}$) and the number of antennas ($N_{\rm ant}$) over increasing bandwidth (B). This insight strongly favors a "large-N, small-D" aperture array design operating at lower frequencies where a wide field of view is naturally achieved.

The 375-500 MHz Band at OVRO

Based on the optimization strategy, we selected the 375-500 MHz band (the 4th Nyquist zone of our 250 MS/s digitizers) as an excellent compromise. It provides sufficient bandwidth to capture the dispersed sweep of a radio pulse while residing in a frequency range amenable to wide-field antennas. However, a theoretical optimization is not enough; the practical suitability of a frequency band depends entirely on the local radio frequency interference (RFI) environment.

To verify that our chosen band is sufficiently quiet at our intended site, we measured the RFI environment from the roof of the Mayer Control Building at OVRO. We used an ETS-Lindgren 3180 Biconical Antenna (Figures 2.1a, 2.1b) and a Siglent SSA3021X spectrum analyzer. A 15-minute integration, shown in Figure 2.1c, confirms that while there are some narrow-band carriers, the

375-500 MHz band is largely free of strong, wide-band interference. This clean band allows us to use the full 125 MHz of bandwidth, maximizing our sensitivity and validating our choice.

(a) Biconical Antenna - Side View

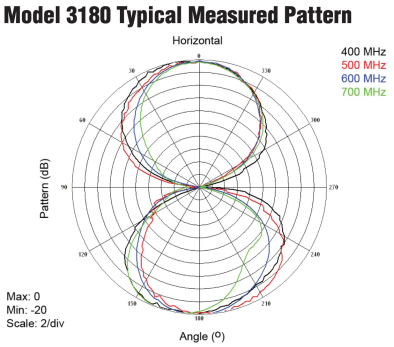

(b) Biconical Antenna - Perspective View

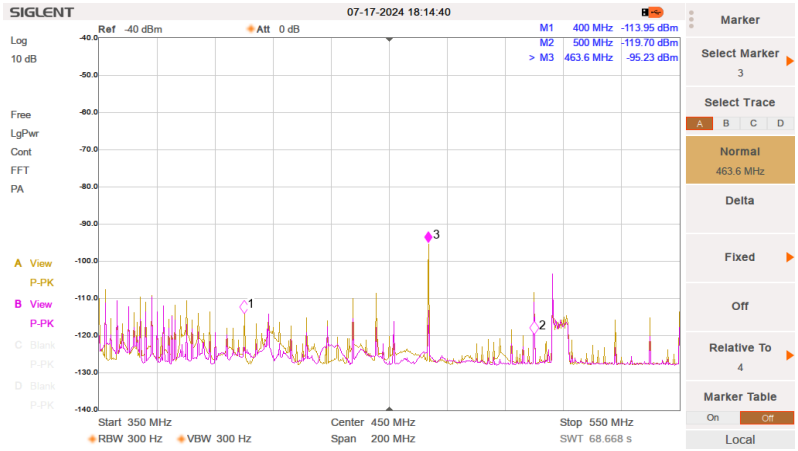

(c) Measured RF spectrum at OVRO.

Figure 2.1: Measurement of the RFI environment at the Owens Valley Radio Observatory, confirming the 375-500 MHz band is relatively free of strong interference.

Chapter 3

LITERATURE REVIEW

The CASM antennas were designed from the shoulders of some other giant radio projects. In this chapter, we review the antenna designs which inspired and informed our own.

3.1 The cloverleaf antenna: a compact wide-bandwidth dual-polarization feed for CHIME

The Canadian Hydrogen Intensity Mapping Experiment (CHIME) is an array of four 100-meter-long cylindrical radio reflectors located in the Canadian province of British Colombia. It has a field of view of more than 200 square degrees and bandwidth spanning 400-800 MHz. (Collaboration et al., 2021). A series of 256 evenly spaced dual-polarization dipole antennas populates the focal point of each cylindrical reflector, for a total of 1024. The antennas (Figure 3.1(a)) are cloverleaf-shaped in order to maximize bandwidth, and the four “petals" are impedance matched with microstrip baluns on the “stem" to form two linearly polarized, 50Ω outputs. These components are fabricated onto PCBs and soldered together for both electrical and mechanical connectivity (Deng, 2012).

This design is good because PCBs can be manufactured in bulk with precise and consistent dimensions for reasonably cheap. It also uses a very elegant matching system with the microstrip baluns (Figure 3.1(b)), avoiding the use of an external or surface mount core-and-wire balun which would increase the antenna’s insertion loss (and thus noise figure) by 0.5 dB or more. Its FoV is also sufficiently wide, as it needs to illuminate all of the cylindrical reflector.

However, CHIME’s use case does not have nearly as strict a noise temperature requirement as CASM. While they can get away with their feed being completely passive, we will need to place our LNAs as close to the antenna output as possible. We can’t afford the loss from the extra electrical length of the PCB baluns, so our antenna itself will need to be matched to 50Ω.

As Deng, 2012 mentions, some iterations of the cloverleaf antenna have experimented with improving the noise figure by placing differential LNAs directly at the top of the stems (Figure 3.1(c)). In theory, this should improve performance by combining all of the potentially lossy impedance matching into the first stage of amplification. However, it actually results in extreme sensitivity to discrete component tolerances in the matching network and thus irregular and asymmetric beam patterns. They attribute this effect to the differential LNA’s inability to sufficiently balance currents across the dipole elements.

3.2 The HIRAX Active Cloverleaf Antenna

The Hydrogen Intensity and Real-time Analysis eXperiment (HIRAX) is a planned array of 1024 6-meter parabolic radio dishes for the Square Kilometer Array site in South Africa. They opted to build on the progress of CHIME’s cloverleaf antenna, which has a sufficient beam width to illuminate the whole of the dish when mounted at the prime focus. They also gave the differential LNA topology another try in order to reduce their overall noise figure (Newburgh et al., 2016), Figure 3.2(a).

Ultimately, HIRAX ran into the same issues with the cloverleaf feed as CHIME did. The shape of the beam in the E- and H-planes was found to be quite uneven, with too small an opening angle in the

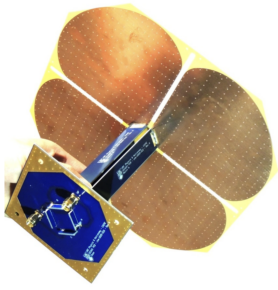

(a) Cloverleaf antenna design.

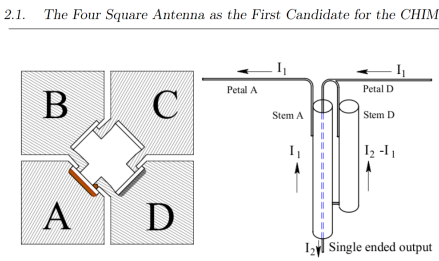

(b) Microstrip balun diagram.

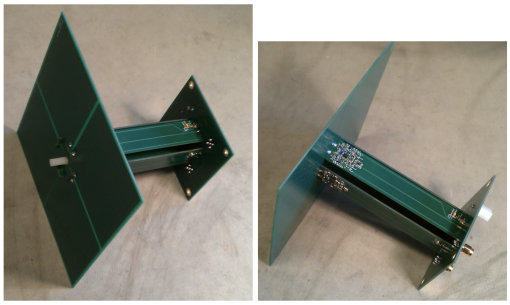

(c) Differential LNA placement.

Figure 3.1: CHIME antenna components: (a) Cloverleaf antenna, (b) balun diagram, and (c) differential LNA configuration.

E-plane and an unacceptably large one in the H-plane. They addressed the latter issue by mounting the cloverleaf feed in the center of a cakepan (Figure 3.2(b)). The differential LNA still presented the same current balancing issue, with a Y-factor test measuring a noise temperature of 60 K when it was designed for a maximum of 30 K (Kuhn et al., 2022).

Therefore, we conclude that the cloverleaf antenna is not a good choice for the CASM project. The extra components required for beam shaping and the inability to achieve the required noise temperature are dealbreakers.

3.3 ARTE's Ultra-Wideband Dual Polarization Antenna Array

The Astronomical Radio Transients Experiment (ARTE) is a galactic FRB localization project at Universidad de Chile. Its constraints are much different from CASM's — with a targeted band of 1200-1800 MHz, a field of view limited to the plane of the Milky Way, and intended deployment on an equatorial mount — but the antenna design is very promising nonetheless. It is based on a structure proposed in Sun et al., 2018 for a fully planar, dual-linearly-polarized dipole antenna centered at 2400 MHz.

In Gallardo et al., 2025, a scaled-up version for ARTE's lower-frequency band is presented. The antenna itself consists of a 2-layer PCB mounted about $\lambda/4$ above a ground plane. There are two sets of dipoles for each linear polarization (shown in Figure 3.3(a)) which are fed in parallel by a microstrip line. This printed dipole shape can be tuned to a specific input impedance by changing parameters like the width of microstrip and the slotline between the dipole elements (Li et al., 2009), allowing the input to the microstrip feed line to be matched to 50Ω.

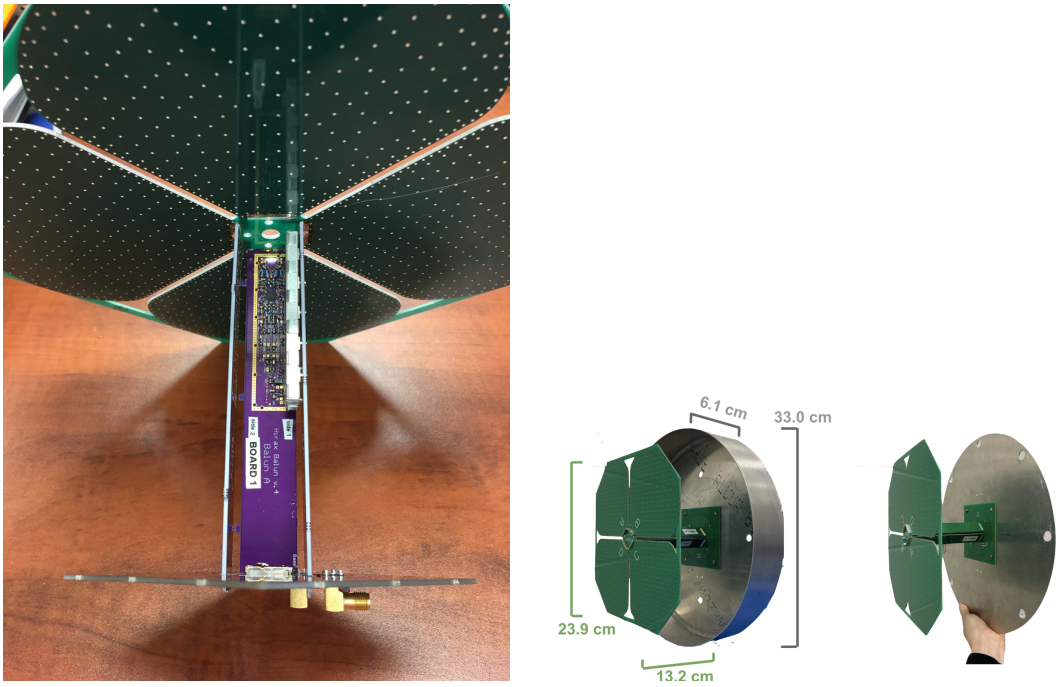

(a) The HIRAX design embeds a first-stage differential LNA directly into the antenna balun.

(b) Cloverleaf feed mounted in a cakepan ground plane to shape the beam.

Figure 3.2: HIRAX antenna design modifications: (a) Differential LNA integrated into the balun, and (b) cloverleaf feed with a cakepan ground plane.

The ARTE PCB dipole array (Figure 3.3(b)) performed very well in initial measurements, agreeing with simulations of S-parameters (Figure 3.3(c)) and array beam pattern. This is encouraging because it shows that the design can be scaled to lower frequencies and still behave as expected. The main difficulties with this design are how to deal with the crossing of the two microstrip feed lines and how to attach coaxial cables without impacting the antenna performance. ARTE used a pair of vias on the PCB for the former, but struggled with the latter due to their use of U.FL connectors which do not provide stable physical connections. Applied to CASM's frequencies, the former would likely remain an issue, but the latter should be addressable with vertical SMA connectors which are electrically small enough.

3.4 Long Wavelength Array (LWA)

The Long Wavelength Array (LWA) is remarkably similar to CASM, with the major exception being the targeted frequency. LWA is an aperture array of 256 dual-polarization antennas stationed at Owens Valley Radio Observatory and the site of the Very Large Array in New Mexico. It operates in the range of 10-88 MHz, which comes with its own unique challenges (sky noise, RFI from FM radio stations, coupling to soil underneath the ground plane) but otherwise has comparable requirements for FoV and bandwidth (Hicks et al., 2009).

Their solution consists of four metal dipole arms electrically and mechanically connected to a central PCB which contains the amplification circuitry (Figure 3.4(a)). Power is supplied with a DC bias voltage on the RF output connector of the PCB. The dipole arms are folded downwards at a 45° angle to achieve the desired impedance match, and the whole structure is mounted above a chicken wire

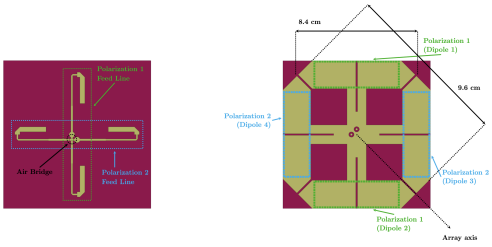

(a) ARTE antenna dipole configuration (4 dipoles, 2 in parallel for each polarization).

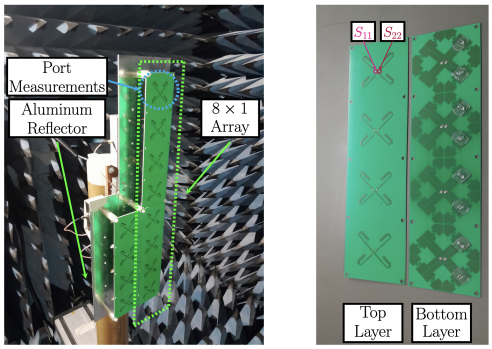

(b) The ARTE PCB dipole array.

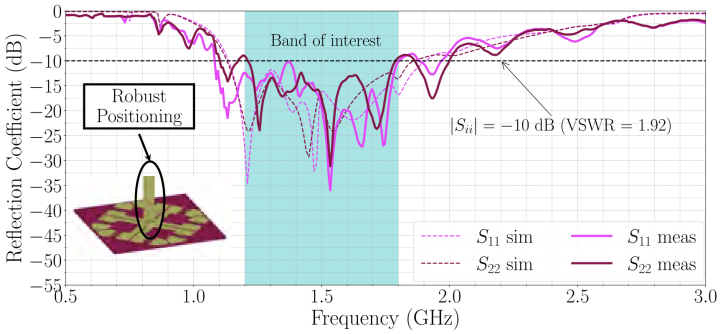

(c) Simulated S-parameters for the ARTE antenna.

Figure 3.3: Details of the ARTE ultra-wideband dual polarization antenna: (a) dipole layout, (b) PCB dipole array, and (c) simulated S-parameters.

ground plane.

The bowtie shape of the dipole arms helps to increase bandwidth (Figure 3.4(b)). In terms of FoV, the LWA antenna is also quite optimal with a wide and symmetric beam pattern shown in Figure 3.4(c). Therefore, we will base the first prototype of the CASM antenna on the LWA design, since the dipole arms can be swapped out independently of the amplifier circuit, allowing for maximum modularity.

A disadvantage of this design is the inability to test the antenna parameters directly with a network analyzer. This is because the signal from each individual dipole arm is amplified separately before being combined with a balun — the same issue encountered by CHIME and HIRAX with their integrated differential LNAs. For LWA, this is less of a concern since the dipoles are electrically large compared to the amplifier PCB, but it might prove to be more challenging when scaling to 400 MHz for CASM.

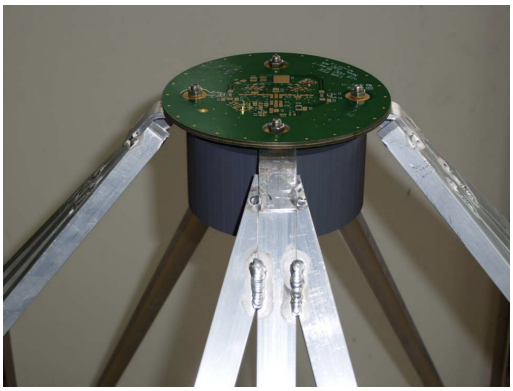

(a) LWA antenna: central PCB with amplification circuitry and connected dipole arms.

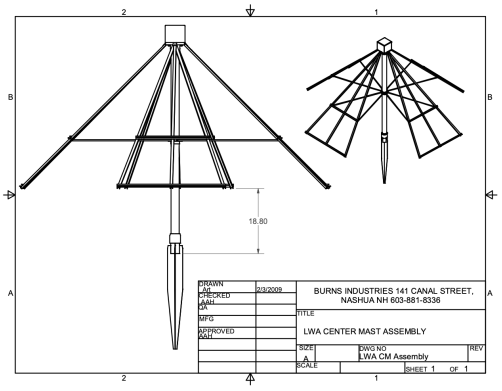

(b) Detail of the LWA bowtie-shaped dipole arm, designed for increased bandwidth.

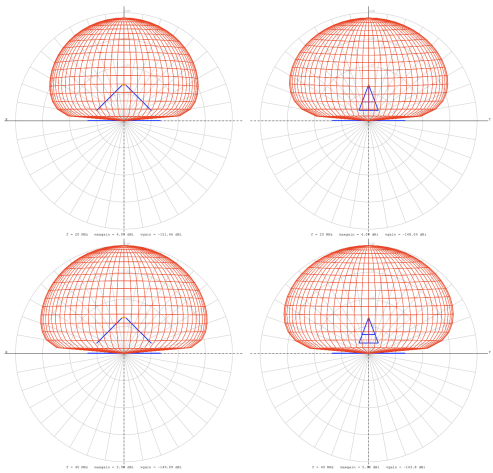

Figure 2.4. E and H plane patterns at 20 MHz (top) and 40 MHz (bottom). The scale is logarithmic total power with 10 dB per division. E-plane patterns are on the left and H-plane patterns are on the right.

(c) Wide and symmetric beam pattern of the LWA antenna.

Figure 3.4: Key aspects of the Long Wavelength Array (LWA) antenna design: (a) overall structure with central PCB, (b) bowtie dipole arm detail, and (c) antenna beam pattern.

Chapter 4

CASM ANTENNA EVOLUTION

4.1 CASM-6

The first prototype for the CASM analog front end (Figure 4.1) was developed during Summer 2024. It was based on the LWA's bent-dipole antenna and optimized for the frequencies of 420-500 MHz. Six units of this revision were fabricated, but they were never tested in array configuration since the antenna's forthcoming flaws made a full redesign more expedient. This prototype primarily provided a learning process for electromagnetic simulation, PCB layout, and surface-mount soldering, as well as an initial investigation into the quirks of the MiniCircuits PMA2-63LN+ amplifier.

Mechanical

Each CASM-6 antenna consists of two independent dipoles and analog front end PCBs, one for each linear polarization. The antenna design centers around custom aluminum quarter-wavelength elements structurally and electrically connected to the PCB with the LNA and balun. The PCBs are mounted back-to-back and rotated 90° relative to one another, allowing the dipole elements and coax connectors to pass through cutouts in the irrelevant PCB.

This front end assembly is mounted onto a 3D-printed frame with a PVC pipe mast to hold it above a chicken wire mesh ground plane. The showerhead-shaped frame is designed for the PCB to securely snap into and easily snap out of, as well as to provide vertical space for proper mating of the SMA connector on the coax. The base for the antenna mast is also 3D-printed and given holes through which to nail tent stakes for stability.

The electrical connection between the dipole elements and the PCB is formed through stainless steel M5 bolts with lock-washers to break through any outer oxidation layers on the aluminum dipole elements. The bolts, along with 3D-printed spacers, hold the elements at an offset above the PCB. This was a later design change to improve the impedance match of the elements by accounting for the electrically large ground plane of the PCB itself. The assembly is shown in exploded view in Figure 4.2.

The lengths of the PVC pipe, aluminum elements, and the height of the 3D-printed spacers were tuned to improve the impedance match of the antenna. That process will be described subsequently.

Signal Path

The first step in designing the signal path was choosing the first-stage LNA. The ideal component would have a noise figure of $\leq$ 0.5 dB ($\approx$36 K), at least 15 dB of gain, and not require a custom external matching network. Out of the available components in the MiniCircuits catalog, the best one fitting those criteria within our frequency range was the PMA2-63LN+, which has a 0.5 dB noise figure, 24 dB of gain, and contains an internal matching network. For simplicity, we also opted to use this chip for the second amplification stage on the front end.

One disadvantage (for this application) of the PMA2-63LN+ is its operating frequency range, 400-6000 MHz, which is much larger than our targeted range. To prevent high-frequency signals

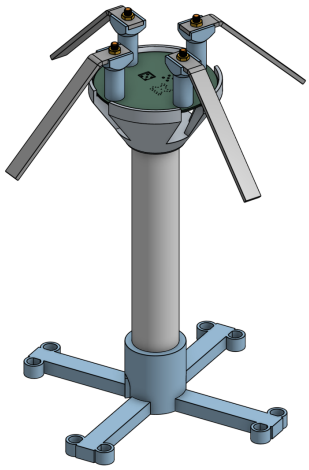

Figure 4.1: Mock-up of one element of the CASM-6 prototype array. Ground plane not shown.

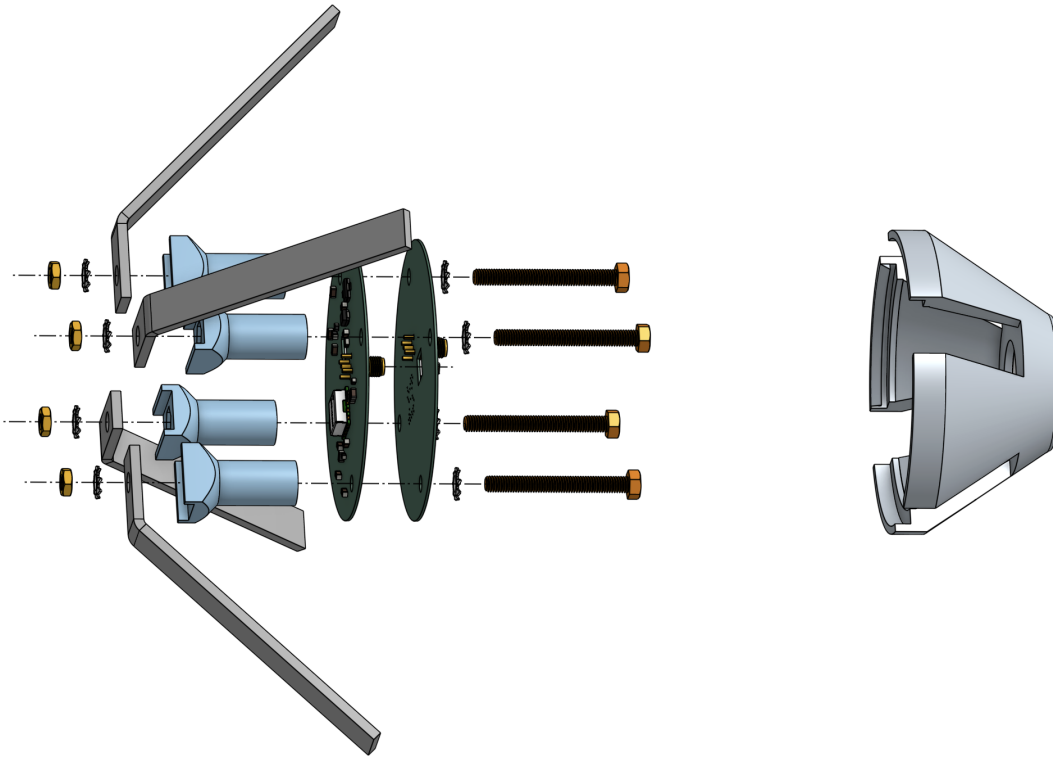

Figure 4.2: Exploded view of CASM-6 front end assembly

(especially RFI from cell towers and WiFi) from propagating through the amplifier chain and potentially overloading it, a filter is necessary to attenuate frequencies above 500 MHz between the two amplification stages. We chose the MiniCircuits RBPF-485+ which has a passband of 435-535 MHz.

The full signal path of the CASM-6 analog front end is diagrammed in Figure 4.3. Its defining trait is the LNA-before-balun topology. Instead of immediately converting the balanced signal across the

two dipole elements to a ground-referenced unbalanced signal (as the passive CHIME and ARTE antennas do), CASM-6 treats the signal from each pole as its own ground-referenced unbalanced signal and independently amplifies them. This also enables us to use a compact 180° hybrid coupler (MiniCircuits SYPJ-2-13+) instead of a typical quarter-wave balun, since the 180° couplers use somewhat lossy core-and-wire technology. The SYPJ-2-13+ has up to 1.8 dB of insertion loss at 500 MHz, meaning using it before any amplification would result in a noise temperature >150 K.

An important consideration of this topology is that each pole of the dipole must be independently matched to 50 Ω with respect to ground. This is because the PMA2-63LN+ expects the input impedance to be 50 Ω in order to achieve its specified noise figure. Satisfying this criterion as well as the FoV constraint proved very difficult for this design, as will be discussed subsequently. Choosing another LNA with a different input impedance could relax this criterion. At the extreme, the LNA and the antenna could be co-designed to match to an arbitrary value. Alternatively, a differential LNA could be designed which would eliminate the need for a balun entirely, but would likely replace it with a bulkier matching network using more passive components, in addition to the issues with differential LNAs encountered by CHIME and HIRAX (discussed in chapter 3).

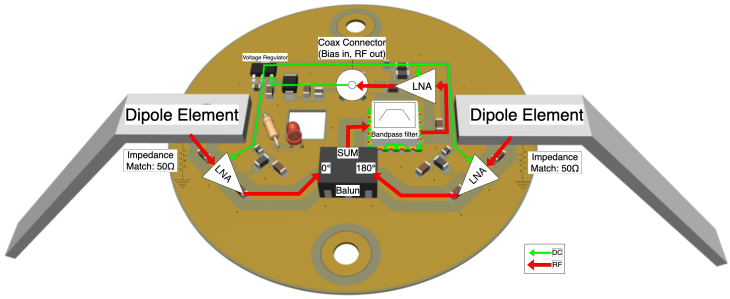

Figure 4.3: Simplified block diagram of the CASM-6 analog front end.

Electrical

The signal path for one polarization is arranged on the top layer of a two-layer PCB with diameter 88 mm, thickness 0.8 mm, and material FR-4. Since two of these PCBs need to be placed back-to-back in the antenna, all the surface-mount components need to be kept on the top side, and the other side is used as a ground plane. The top layer is also filled in with copper to form coplanar waveguides, using trace width of 1.5 mm and gap of 2.5 mm to create 50Ω transmission lines.

Each PMA2-63LN+ amplifier draws about 50 mA at 5 V supplied to its RF-out pin through an external bias tee on the PCB. 5 V power is provided to the amplifiers through a linear regulator, which in turn gets its power through a reverse-polarity protection diode and a bias tee on the output coax connector. The back end signal conditioning board, discussed in the next chapter, provides bias voltage over the coax cable.

The full schematic and bill of materials for the CASM-6 front end is in Appendix B.

Fabrication Strategy

The base, PCB attachment, and PCB offset components are 3D printed from PLA plastic. The central shaft is cut from 1.5" PVC pipe. The dipole elements are cut from aluminum bar stock. A reasonable starting point is 1/2” wide by 1/8” thick rectangular stock, which is readily available from McMaster-Carr and is easy to work with. The dipole elements are attached with M5 screws, nuts, and lock washers to make a secure electrical connection.

For maximum consistency, the dipole elements themselves are cut down from bar stock using a 3D printed jig, which has openings through which to center punch and score the drill hole, bend point, and cut (Figure 4.4(a)). Then they are shaped into a 45° bend angle using a hammer, vice, and another 3D-printed jig (Figure 4.4(b)). In theory, the elements should be angled down at about 45° from horizontal in order to achieve a resonance at 50Ω. We could fine-tune the impedance by adjusting this angle, but even with the jig, precision is hard to obtain with the hammer and vice method. So we set this angle as a fixed parameter of the design.

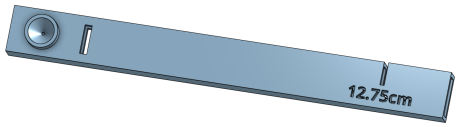

(a) 3D printed jig for marking drill holes, bend points, and cuts on dipole elements.

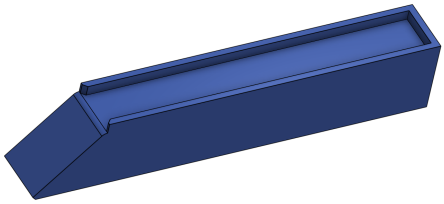

(b) 3D printed jig used with a hammer and vice for bending dipole elements to a 45° angle.

Figure 4.4: 3D printed jigs used in the fabrication of dipole elements: (a) jig for marking cutting and drilling points, and (b) jig for achieving the 45° bend angle.

Simulation Process

In order to actually make the antenna work, we need to tune the shape and placement of the dipole elements. The goal is to match each pole to an impedance of 50Ω with respect to the PCB ground, since that is what the PMA2-63LN+ expects. As-yet unconstrained parameters of this design are diagrammed in Figure 4.5.

The values of `r0` and `r1` are constrained by the size of the circuit board, which was being designed at the same time, so we fixed them at a reasonable estimate of 2.5 cm and 5.0 cm, respectively. `w1` and `t2`, the dimensions of the bar stock we purchased, are also fixed. Remaining tunable parameters are shown in green in Figure 4.5.

We started with a dipole element length of `bl` = $\lambda/4$ = 15 cm and elevation from ground plane of `h` = $\lambda/2$ = 30 cm. In later simulations, we also added an offset between the antenna elements and the circuit board (`pcboffset`) after realizing the ground plane of the circuit board will modify the dipole radiation pattern. These are the primary variables over which to optimize since they are the easiest to change (by printing/cutting different lengths).

A parametric model of the conductors of the antenna design was made with ANSYS High Frequency Structure Simulation (HFSS) software. The design was simulated over the variable ranges in Table

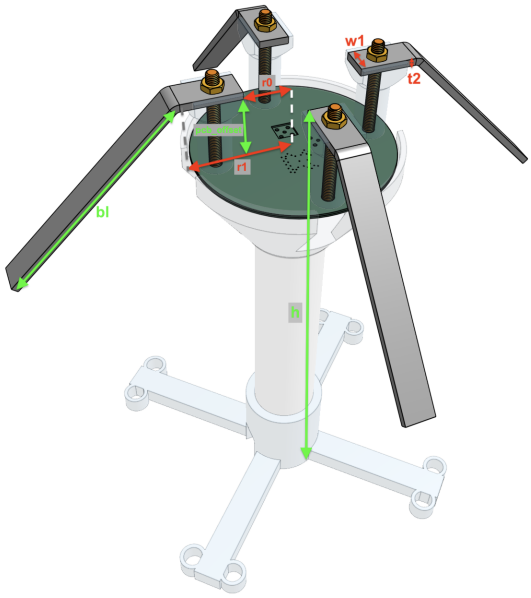

Figure 4.5: Tunable parameters of the CASM-6 antenna. `w1` = width of dipole element, `t2` = thickness of dipole element, `r0` = radius of inner edge of dipole element, `r1` = radius of bend of dipole element, `bl` = bend length of dipole element, `pcboffset` = distance between top of PCB and bottom of dipole element, `h` = distance between ground plane and bottom of dipole element

4.1, and each combination of variables was evaluated using the benchmarks in Table 4.2. Details of the HFSS settings used for these simulations are provided in Appendix A.

Variable	**Description**
h	Linear Step from 20cm to 38cm, step=3cm
bl	Linear Step from 8cm to 16cm, step=2cm, Single Value at 9cm
pcboffset	Linear Step from 20mm to 50mm, step=5mm

Table 4.1: CASM-6 Design Parameters – Values Simulated

Variable	**Description**
logmag(S_{11})	≤ -10 dB from 435-485 MHz
log10(RealizedGain($\theta = 0, \phi = 0$))	≥ 3 dB
log10(RealizedGain($\theta = 90°, \phi = 0$))	≤ 0 dB
Beam Width at log10(RealizedGain($\theta = 0, \phi = 0$)) - 3 dB	120° ± 15°

Table 4.2: CASM-6 Simulation Benchmarks

Preliminary Simulations without PCB

In the interest of starting with as little complexity as possible to understand the behavior of the software, we began with simulating only the dipole elements and the mesh ground plane. Instead of using a 50 Ω port between each pole and ground, we used a 100 Ω port between each pair, which is

equivalent to two differentially-driven (in series) 50 Ω ports. The HFSS model is shown in Figure 4.6.

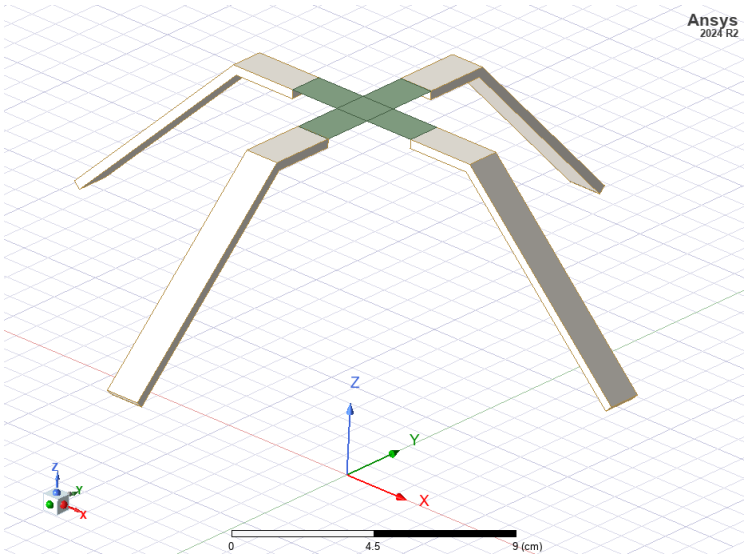

Figure 4.6: Simplified HFSS model of the CASM-6 antenna without the PCB. Green rectangles are 100 Ω ports.

The simplified design was simulated with a range of `h` and `bl` values. Logmag(S_{11}) vs. frequency is plotted for each configuration in Figure 4.7. The optimal configuration, the red line reaching a minimum of -28 dB at around 462 MHz, has `h` = 13 cm and `bl` = 9 cm. We used this as the starting point for the next set of simulations.

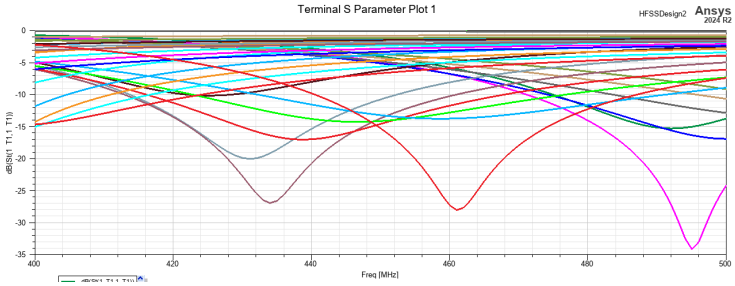

Figure 4.7: Simulated logmag(S_{11}) of the simplified CASM-6 antenna variations.

Parametric Simulations of the Full Design

A new HFSS model (Figure 4.8) was made including the ground plane of the PCB and bolts of length `pcboffset`. This time, each pole was given its own independent port referenced to the PCB ground plane, allowing more direct verification of the 50 Ω match. The model was simulated for all variations in the parameter space from Table 4.1. As a starting point for identifying the best configuration, the frequency-dependent S-parameters for all variations are plotted in Figure 4.9.

The deepest blue spike reaching a S_{11} of -63 dB is the configuration with `bl` = 9 cm, `h` = 23 cm, `pcboffset` = 3.5 cm. Figure 4.10 shows the polar gain plot at 475 MHz for that winning

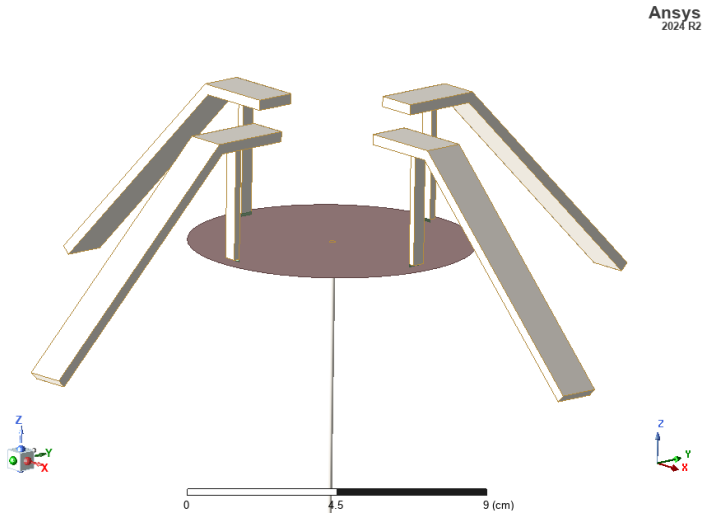

Figure 4.8: HFSS Model of the full CASM-6 antenna design. Green rectangles are 50 Ω ports. Ground plane not shown.

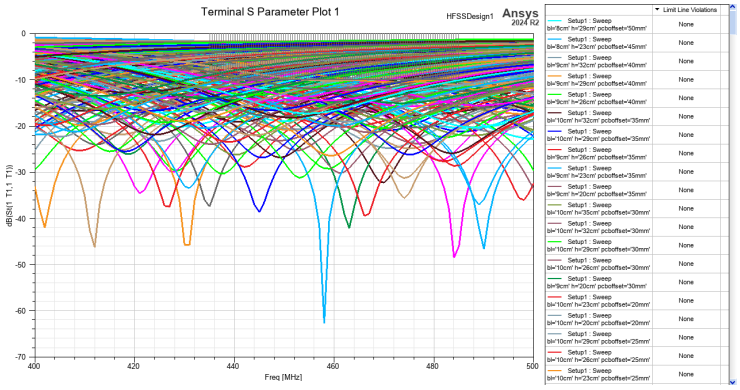

Figure 4.9: Frequency-dependent S-parameters for all simulated variations of the full CASM-6 antenna design.

configuration. It has a zenith gain of 6.34 dB, a FoV opening angle of 120°, and gain < 0 dB for elevations < 18°. This satisfies all of the benchmarks!

To test the sensitivity of the design to variations in the other two parameters, several perturbations were simulated. `h` was varied from 30 cm to 40 cm and `pcboffset` from 1.9 cm to 2.9 cm. Resulting S_{11} curves are shown in Figure 4.11, and the polar gain plots (again at 475 MHz) for the same family of configurations are shown in Figure 4.12. I'm sufficiently satisfied that this configuration is robust enough to perform even with fabrication tolerances.

Lessons Learned

As previously mentioned, a variety of difficulties encountered with the CASM-6 antennas meant they never saw the sky before work was started on the next revision. Still, developing this design provided several important lessons:

- **Surface-mount soldering is hard.** The PMA2-63LN+ chips, only 2×2 mm, proved especially painful to get right. The stencil we ordered was too thick and applied too much solder paste

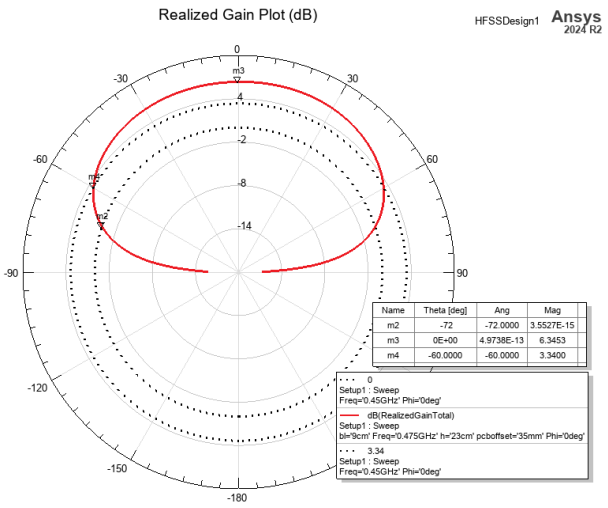

Figure 4.10: Polar gain plot at 475 MHz for the optimal CASM-6 configuration (`bl`=9 cm, `h`=23 cm, `pcboffset`=3.5 cm).

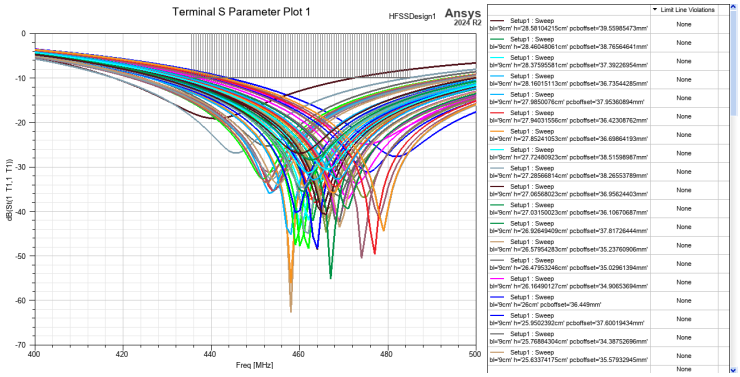

Figure 4.11: Simulated S_{11} curves showing sensitivity to perturbations in `h` and `pcboffset` around the optimal configuration.

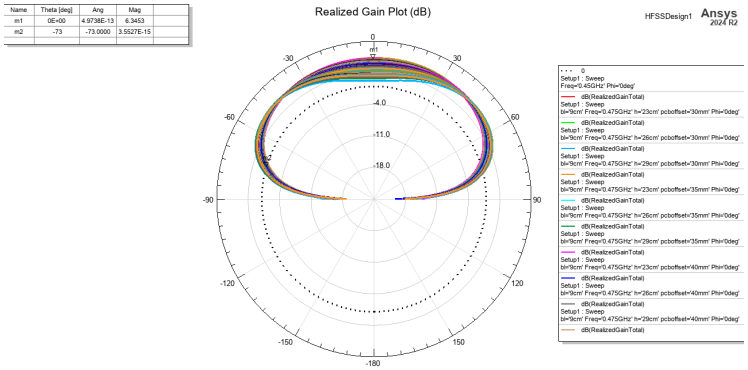

Figure 4.12: Polar gain plots at 475 MHz for CASM-6 configurations with perturbations in `h` and `pcboffset`.

to the pads, resulting in some adjacent pads on the amplifier getting shorted together during reflow (see Figure 4.13). These required manual rework, which was extremely time-consuming. Lesson learned: use a thinner stencil, or pay extra for PCB assembly by the fab.

- **PMA2-63LN+ are extremely ESD-sensitive.** At least, that seems the most likely explanation for why more than half of the PCBs we assembled spontaneously broke between tests. “Broke" in this case means the PCB started drawing substantially more or less than the expected 150 mA, with a corresponding drop in the RF power output. The root cause turned out to be a seemingly random subset of the amplifiers which had failed or shorted internally. Replacing the broken amplifiers (again, a very time-consuming process) restored the PCBs to expected operation. Lesson learned: the PMA2-63LN+ is a very fickle device and should probably be replaced with a different amplifier in future revisions.

- **Too many parts.** Each antenna requires assembly of a non-trivial configuration of fasteners and custom components. That includes the dipole elements, which also have to be cut to length, drilled, and bent. The total time to assemble 6 antennas was at least 12 hours, which is not acceptable at scale. Lesson learned: integrating the dipole into the PCB itself, like CHIME and ARTE did, would be highly preferable for future revisions.

- **The LNA-before-balun topology is problematic.** Amplifying each pole of the dipole in this single-ended fashion is a fine idea in theory for reducing T_{sys}, but using an amplifier that's already internally matched to 50 Ω adds unnecessary constraints for the antenna design and limits its bandwidth. It would be better to co-design a LNA with the dipole to match at a more mutually favorable impedance value. Additionally, amplifying the dipole poles before balancing makes it impossible to independently test the passive and active parts of the antenna with a VNA. With this topology, evaluating the performance of early prototypes is very difficult. Lesson learned: integrating a passive balun into the dipole itself, like CHIME and ARTE did, would be highly preferable for future revisions.

4.2 CASM-256

The second revision of the CASM analog front end (Figure 4.14) was designed in Winter 2025 and involved significant modifications to optimize for scalability to 256 antennas. To decrease the number of parts and integrate a passive balun before the LNA, we decided to adapt the two-layer PCB antenna used by the ARTE array. Five prototypes were fabricated in Spring 2025. Empirically measured S-parameters of individual antennas agree well with simulation, but they have not yet been tested in array configuration due to ongoing difficulties with the digital back end. Still, simulation results are promising enough that we plan to proceed with this design for the full CASM-256 deployment at Owens Valley Radio Observatory.

Printed Dipole

Similar to ARTE's PCB antenna, the CASM-256 antenna is based on the designs proposed in Sun et al., 2018 and Li et al., 2009. Each polarization of the antenna is formed from two “printed dipoles" fed in parallel. Figure 4.15 shows the equivalent circuit diagram for one printed dipole.

Constraints for the CASM-256 application include a bandwidth of 375-500 MHz and a 50 Ω input impedance at the feed point (location where the two feed lines from the two printed dipoles converge). We choose 0.8 mm thick FR-4 for the PCB substrate to minimize both cost and dielectric loss. The center frequency constrains the length ($\lambda/2$ = 34 cm) of the dipole. The desired input impedance of 50 Ω means the impedance of each microstrip feed line (red in Figure 4.16) needs to be 100 Ω since

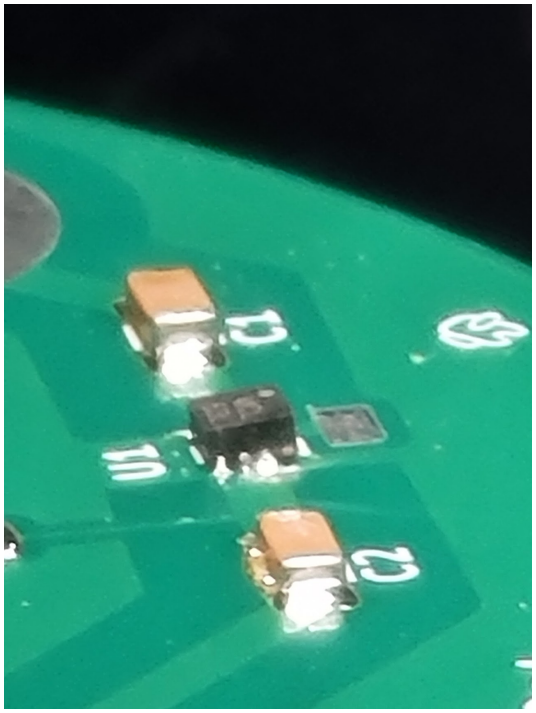

Figure 4.13: Microscope view of a CASM-6 PCB. The PMA2-63LN+ chip, marked U1 on the silkscreen, is supposed to have four separate solder connections to the board (on the side facing the camera). This one came out of the reflow oven with just three, and two of them were shorted together. Manually reworking this took nearly 30 minutes.

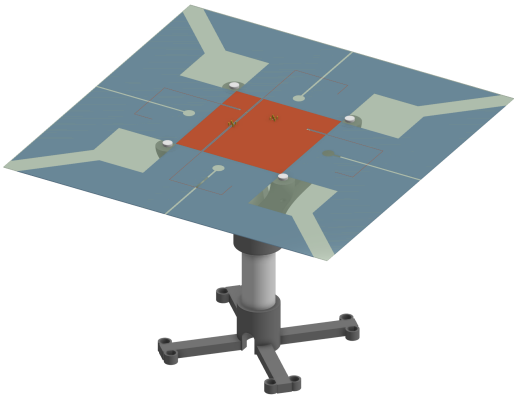

Figure 4.14: Antenna assembly for CASM-256. Top and bottom sides of the antenna PCB are colored red and blue, respectively.

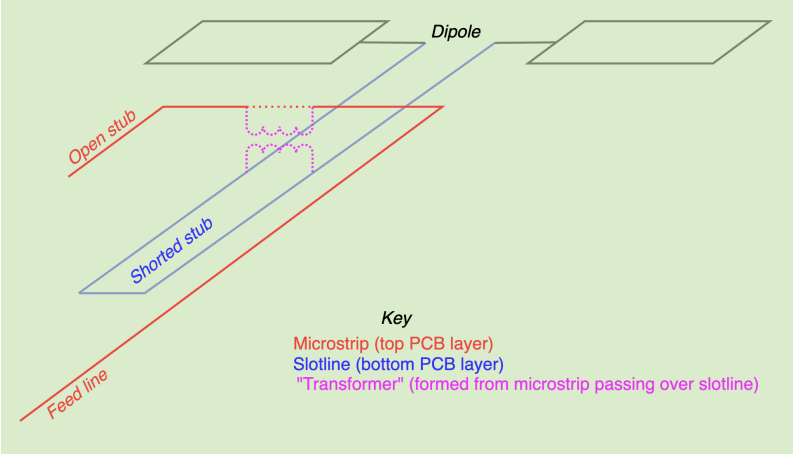

Figure 4.15: Circuit representation of the printed dipole feed network. Microstrip ground plane not shown.

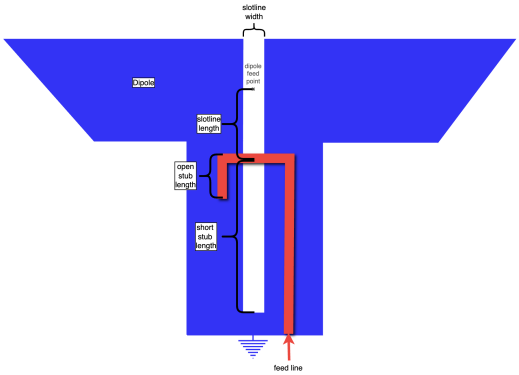

Figure 4.16: Physical realization of the printed dipole feed network. Tunable parameters are labeled. Red and blue represent the top and bottom layers of the PCB, respectively.

there are two of them in parallel. Together with the substrate thickness, this constrains the width of the microstrips to 0.3 mm.

This leaves the length of the open stub, the length of the shorted stub, the width of the slotline, and the total length of the slotline as free parameters to tune (shown in Figure 4.16). Li et al., 2009 provides analytical equations for these parameters (see Appendix C) in terms of the desired impedances. The equations depend on knowing the characteristic impedance of the slotline; equations for that are given in Garg, Bahl, and Bozzi, 2013, but they are only valid for substrates with very high dielectric constants ($\varepsilon_r \approx 9$) and much higher frequencies (much higher ratio of slotline width to wavelength).

To proceed with the analytical method, we would need to determine the characteristic impedance of the slotline through simulation. While this is definitely worth doing, we were under a time constraint for producing a physical prototype, so we opted to move on to simulating the whole antenna and running the HFSS optimizer across reasonable values for the tunable parameters. This process is discussed next.

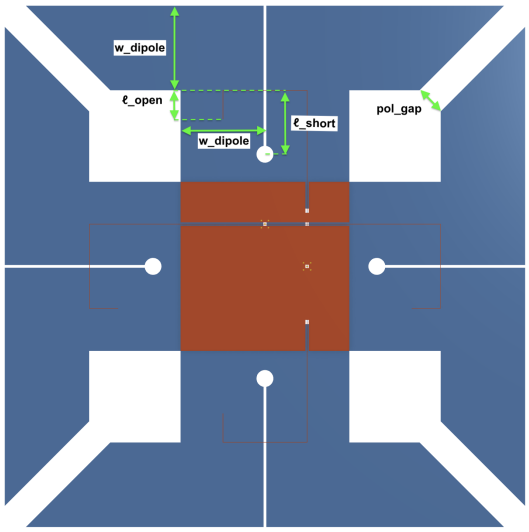

Figure 4.17: Full dual-polarization antenna layout using printed dipoles. Parameters tuned in simulation are indicated with green dimension arrows. Red and blue represent the top and bottom layers of the PCB, respectively.

Simulation Process and Results

The full CASM-256 antenna is formed from four printed dipoles arranged around a central ground patch (Figure 4.17). Feed lines from opposing dipoles are connected together at an SMA connector at their midpoint. To prevent crosstalk between polarizations, we left some space (`pol_gap` in the figure) between adjacent dipoles, resulting in the total side length of the antenna being a bit longer than the length of the dipole.

For one of the polarizations, one microstrip feed line must pass under the other; this was achieved with vias symmetric about the center. (Figure 4.18). This is not an ideal solution since the vias introduce parasitic properties and the crossing of the microstrip feed lines introduces crosstalk between the two polarizations. For this prototype though, it was much easier than soldering on an external air bridge.

The rest of the parameters in Figure 4.17, as well as the height of the antenna off the ground plane, were tuned using the HFSS Design of Experiments (DOE) tool to understand the relative strengths of their relationships to our benchmark quantities (Table 4.3). Some parameters, like the width of the dipole elements, were found not to have meaningful impact on the antenna performance so we fixed them to reasonable, arbitrary values. The chosen values for each parameter are explained in Table 4.4.

Variable	**Description**
logmag(S_{11})	≤ -10 dB from 375-500 MHz
log10(RealizedGain($\theta = 0, \phi = 0$))	≥ 3 dB
log10(RealizedGain($\theta = 90°, \phi = 0$))	≤ 0 dB
Beam Width at log10(RealizedGain($\theta = 0, \phi = 0$)) - 3 dB	120° ± 15°

Table 4.3: CASM-256 Simulation Benchmarks

The optimal configuration satisfies all benchmarks for the upper half of the band. Logmag(S_{11}) is less than -10 dB for both polarization throughout the band (Figure 4.19), indicating an excellent

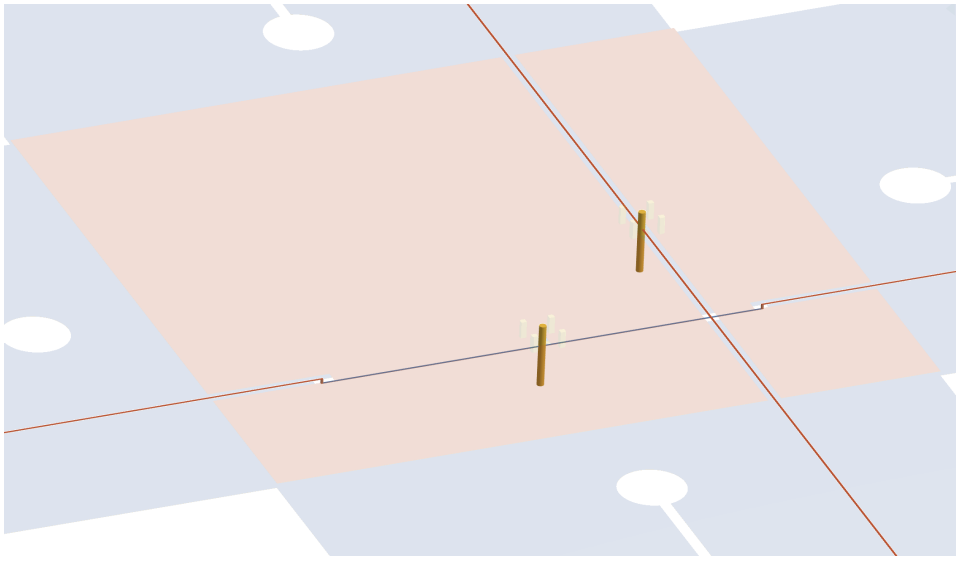

Figure 4.18: Close-up view of the center of the PCB antenna where the two microstrip feed lines cross. Red and blue represent the top and bottom layers of the PCB, respectively.

Variable	**Description**
`pcb_thickness`	Fixed to 0.8 mm (minimize dielectric loss)
`h`	Simulated values between $\lambda_c/4$ = 17 cm and $\lambda_c/2$ = 34 cm. This predominantly affected the beam width of the antenna, with `h` = $\lambda_c/4$ being too narrow and `h` = $\lambda_c/2$ resulting in distortions in the beam shape. The maximum beam width without distortions at any frequency in the band was $\approx \lambda_c/3$, or 24 cm.
w_{dipole}	Simulated values between 1 cm and 10 cm. No significant effects were observed, so it was fixed arbitrarily at 6 cm.
`pol_gap`	Fixed arbitrarily to 2.1 cm.
L_{dipole}	Fixed to $\lambda_c/2$ = 34 cm.
w_{slotline}	Simulated values between 1 and 5 mm. There was no clear overall effect or sense that it had an optimal value independent of the rest of the feed network, so it was fixed arbitrarily to 2 mm.
$w_{\text{microstrip}}$	Fixed to 0.36 mm (100 Ω transmission line with 0.8 mm thick FR-4).
$\ell_{\text{open stub}}$	Simulated between 1 cm and 7 cm. Optimal configuration found at 2 cm.
$\ell_{\text{short stub}}$	Simulated between 1 cm and 7 cm. Optimal configuration found at 4.5 cm.
ℓ_{slotline}	Fixed to w_{dipole} = 6 cm for simplicity.

Table 4.4: CASM-256 Design Parameters. This information is duplicated in the dimensions drawing in Appendix D.

impedance match. Beam width is sufficient for frequencies $\gtrsim$ 450 MHz (Figure 4.20) but drops below 100° in the lower half of the band (Figure 4.21), which trial and error in simulation revealed to be the best available compromise. Raising the antenna higher off the ground plane resulted in distortion to the beam shape in the upper frequencies, and lowering the antenna closer to the ground plane decreased the beam width over all frequencies.

Finding this optimal configuration involved adding a bodge fix to the slotline of the printed dipole — the circular termination to the shorted end. In theory, the sudden widening of the slot causes the termination to act more like an open circuit than a short (Garg, Bahl, and Bozzi, 2013), so it is unclear exactly why this *improved* the antenna performance, but we could not find a configuration

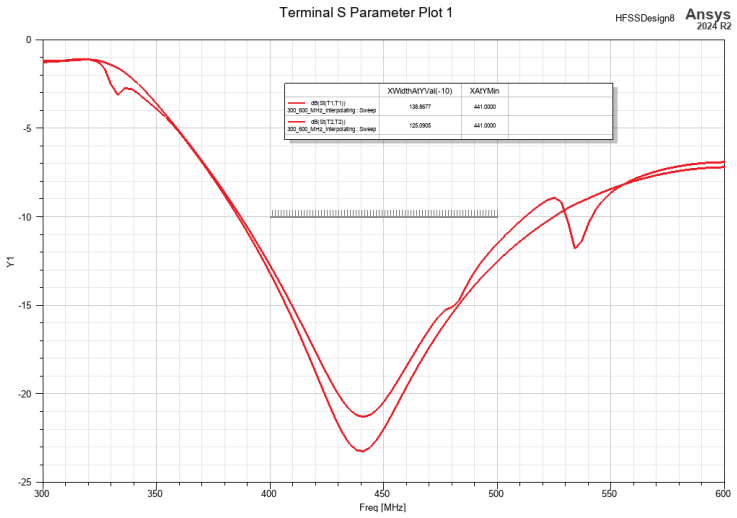

Figure 4.19: Logmag of simulated S_{11} vs. frequency for each polarization of the CASM-256 antenna prototype. Gray hatched line indicates the minimum band for which we want less than -10 dB. Inset table shows full bandwidth for which the S_{11} < -10 dB.

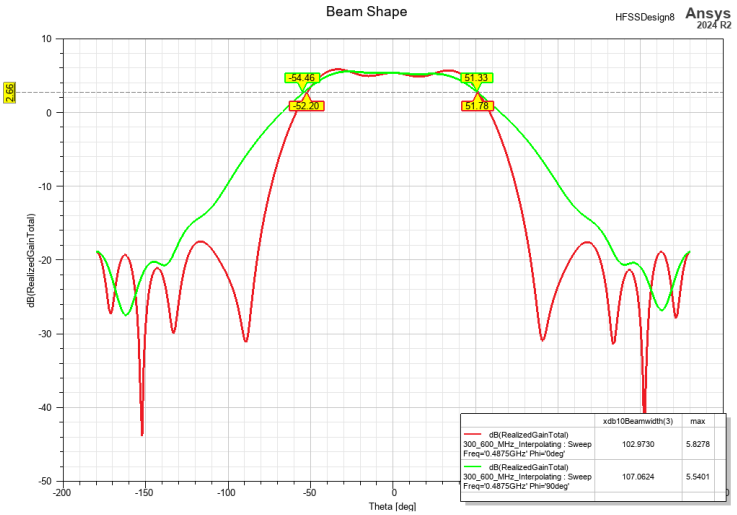

Figure 4.20: Plot of simulated antenna gain in dB vs. angle from zenith in each polarization plane at 487.5 MHz. Inset table shows the FWHM and zenith gain for each polarization.

with a wider bandwidth without it. The bodge fix works for now, but will be revisited in future antenna revisions once the characteristic impedances of the slotline and the dipole itself have been simulated in isolation.

Front End Electronics

We had discussed putting the LNA circuit directly on the antenna PCB, but decided against it for this first prototype in favor of a more modular approach. As shown in Figure 4.22, we added surface mount pads for a custom form factor LNA PCB (5 cm wide) and an SMA connector at the output for both polarizations, one on top and one on bottom. With the final LNA design still in progress, the ability to iterate and test without ordering a new batch of 37×37 cm PCB antennas each time is very useful. We also kept an SMA connector directly at the feed point of each polarization to allow

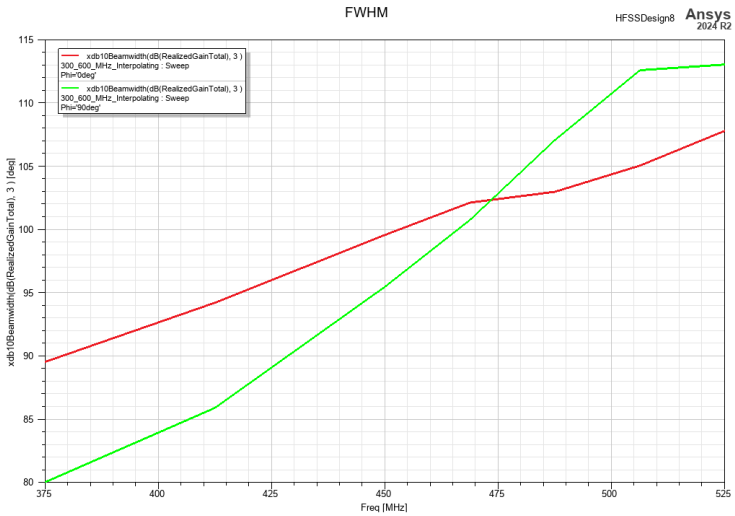

Figure 4.21: Plot of simulated FWHM of antenna beam in each polarization vs. frequency.

measurement of the antenna S-parameters and use of other connectorized amplifiers if desired.

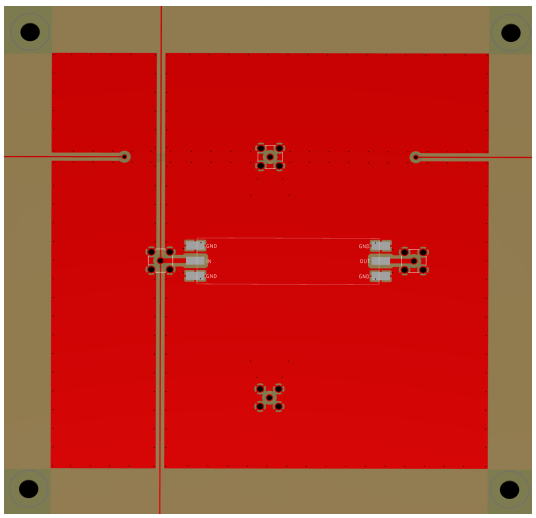

Figure 4.22: Top view of antenna PCB with surface-mount pads and extra SMA connectors added. White silkscreen annotations show the dimensions and connections of the LNA PCB.

For initial testing, we designed another front end PCB using the MiniCircuits PMA2-63LN+ as the LNA. Figure 4.23 shows the circuit board, and the schematic is available in Appendix B. Compared to the CASM-6 version, we removed the band pass filter and added a 3 dB attenuator between the output of the PMA2-63LN+ and the input of the second stage amplifier. We used the MiniCircuits GALI-74+ for the second stage this time because the upper limit of its band is just 1 GHz instead of the PMA2-63LN+'s 6 GHz. The band pass filter was moved to the back end, discussed in chapter 5. A different voltage regulator with an ultra-low 200 mV dropout was used to enable powering the amplifiers with only 5 V input (the amplifiers still operate normally at the resulting 4.8 V). This is desirable since it allows the back end to only generate a single supply voltage for both the front and back end amplifiers, and also makes it possible to do quick and dirty field testing powered from a USB device with a spliced cable.

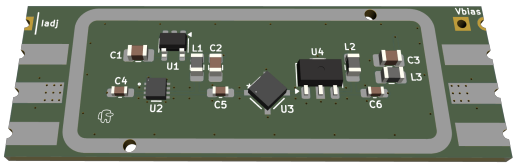

Figure 4.23: Top view of the first revision of the LNA PCB for CASM-256, designed to be soldered onto the antenna PCB. RFI cover not shown.

This PCB was designed for a 1.6 mm thick, four-layer FR-4 stackup. Having four layers instead of two helped with routing power in this relatively small area, and also decreases dielectric loss even further since the copper layers are even closer together than in the two-layer 0.8 mm PCB. A metal cover can be soldered over the components on the top layer, providing robust shielding from RFI. The input and output signals are routed underneath the edges of the cover on the second inner layer between the power and ground planes for even more shielding. The input and output pads are castellated on the edges for surface-mounting onto the antenna PCB, or alternatively are spaced properly for SMA connectors to be soldered on for VNA testing.

Fabrication and Tests

Assembly for this design is significantly easier than CASM-6. The stand base and PVC pipe remain the same from CASM-6. A new 3D-printed part holds the PCB antenna by its four mounting holes. 3D-printed pegs press-fit tightly into the holes. The assembly is shown in Figure 4.24.

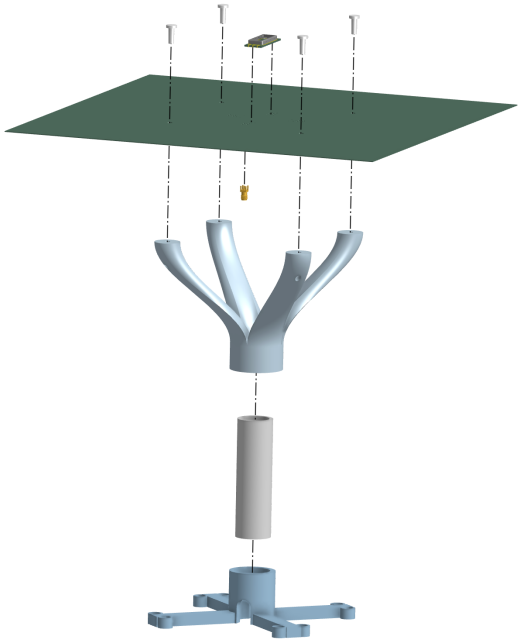

Figure 4.24: Exploded view of CASM-256 antenna assembly

Five antennas were fabricated and taken to Owens Valley Radio Observatory for preliminary testing in March 2025. We set up the antennas and a chicken wire ground plane near the intended array location (Figure 4.25, see chapter 5 for array details). A NanoVNA was used to measure the S_{11} of

the antenna from the coax connector at the feed point; the result (Figure 4.26) agreed nicely with simulations (Figure 4.19).

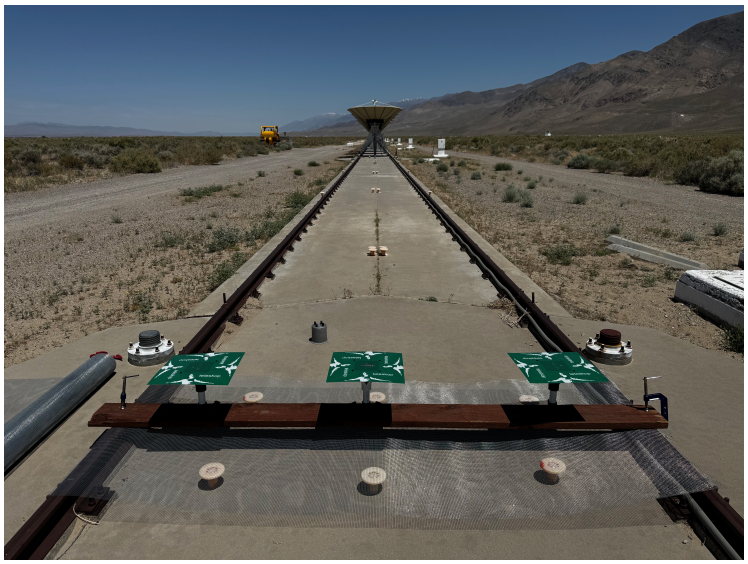

Figure 4.25: Test deployment of CASM-256 antennas and ground plane at the array site, the old railroad track in the middle of the DSA-110 array at Owens Valley Radio Observatory.

Figure 4.26: NanoVNA readout of a CASM-256 antenna prototype on a ground plane at Owens Valley Radio Observatory. Frequency range shown is 100 MHz to 1000 MHz. The reading confirms that the antenna has S_{11} < -10 dB for frequencies 375 - 500 MHz.

We also installed the new front end PCBs and tested the whole analog signal path (Figure 4.27) with a spectrum analyzer. There were significant challenges with both the front and back end amplifier circuits which will be discussed subsequently, but we did manage to get a few good readings (Figure 4.28) before they burned out. This confirms that the antenna is well matched to the 50 Ω LNA and operates within the expected bandwidth.

We had planned to plug two antennas into the digital back end and plot correlations over the course of a day, which would verify that the system is at least able to observe the brightest radio source in the sky — the sun. Unfortunately, the only available test setup for the digital back end had a firmware bug that prevented us from collecting any data while we were at OVRO.

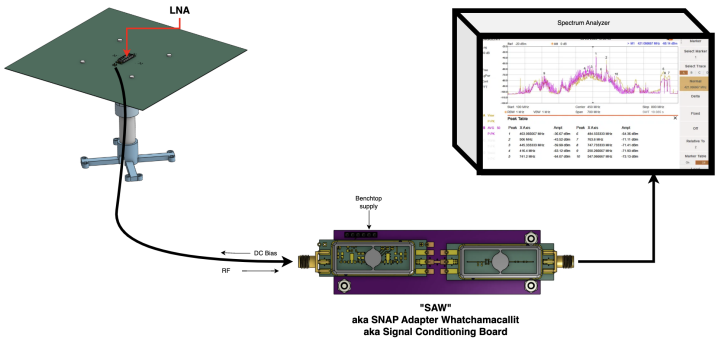

Figure 4.27: Block diagram of the full analog signal path tested at OVRO in March. The back end board, containing a custom 4th-order elliptic filter, is discussed in chapter 5. Full spectrum analyzer readout shown in Figure 4.28.

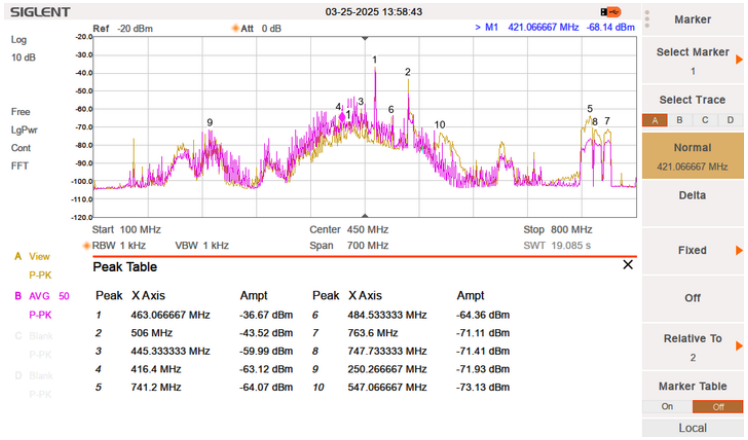

Figure 4.28: Spectrum analyzer view of the power output from the full analog signal path test at OVRO in March. RFI spikes from known sources are present at the expected frequencies (compare to Figure 2.1).

Lessons Learned

Despite the time crunch in which this prototype CASM-256 antenna was designed, it performs remarkably well. The printed dipole has passed the proof of concept with great promise, considering it has not been fully optimized yet. The amplification circuits, however, turned out to be riddled with problems. At least one additional prototype iteration is needed before actually scaling to 256 antennas.

- **0.8 mm FR-4 is floppy.** The 37×37 cm antenna PCBs arrived slightly warped and concave, and stayed that way even when mounted on the 3D-printed stands. This is not acceptable. Lesson learned: the (negligible, as it turns out) extra dielectric loss from thicker substrate is worth the structural integrity. Future iterations will use 1.6 mm FR-4.
- **PLA plastic is not sun-proof.** After a day in the Owens Valley Sun, the 3D-printed antenna stands became soft and yielded to gravity. Lesson learned: 3D printing is not viable for the array deployment. A sturdier mounting method is needed. We have discussed using multiple thin PVC pipes as “table legs".

- **The amplification circuits need more careful design.** We found several problems with the LNA. First, the 3 dB attenuator in between the two amplifiers seemed to completely block all signals, with the LNA reading a gain of < -40 dB across the band. This behavior was consistent across different units. When the attenuator was replaced with a 1 μF capacitor, the gain became +40 dB as expected. Second, the GALI-74+ amplifiers were very prone to burning out; sometimes they can be provoked into a failure mode where the RF OUT / DC IN pin becomes internally shorted to ground. The cause is unclear but is likely something to do with excessive RFI and the removal of the attenuator likely didn't help. The PMA2-63LN+ amplifiers also suffered this issue, with one unit internally shorting immediately upon power-on, and another spontaneously shorted out after several minutes of normal operation. Our best guess is that intense spikes of RFI, known to happen occasionally at OVRO from terrestrial sources, are to blame. Lesson learned: we need to use amplifiers with better dynamic range for future LNAs. In fact, our colleague Saren Daghlian at Caltech is working on designing a custom LNA around the MiniCircuits RF transistor SAV-581+. Initial prototypes have achieved a noise temperature of just 10 K.

- **Desoldering LNA PCBs surface-mounted to the antennas is difficult.** The surface-mount system was designed with modularity and hot-swappability in mind, but swapping the LNA PCBs out requires the whole board to get *really* hot, which is hard to do even with a heat gun. Lesson learned: it'll be easier to just connectorize everything and accept the extra fraction of a dB of loss.

Predicted Array Performance

The ultimate measure of success for the analog front end is the System Equivalent Flux Density (SEFD) of the full 256-element array. As derived in chapter 2, our science goals require an SEFD $\lesssim$ 5 kJy, which in turn constrains the total system temperature to $T_{\rm sys} \leq 50$ K. With the performance of the final antenna design simulated and the next-generation LNA measured, we can now calculate a precise prediction for the performance of the full system.

The total system temperature is the sum of contributions from the sky and the receiver: $T_{\rm sys} = T_{\rm sky} + T_{\rm rec}$. The receiver temperature is dominated by the first stage of amplification, which the new SAV-581+ based design decreases to $T_{\rm LNA} = 10$ K. We will therefore take the receiver temperature to be $T_{\rm rec} \approx T_{\rm LNA} = 10$ K. Adding the average sky temperature of $T_{\rm sky} \approx 25$ K, we arrive at a final predicted system temperature:

$$T_{\rm sys} = T_{\rm sky} + T_{\rm rec} = 25\ {\rm K} + 10\ {\rm K} = 35\ {\rm K}$$

Next, we calculate the effective area, $A_{\rm eff}$, using the simulated gain of the antenna. The relationship between gain and effective area is given by:

$$A_e(\theta, \phi) = \frac{\lambda^2 G(\theta, \phi)}{4\pi}$$

From the simulation results shown in Figure 4.20, the antenna has a zenith gain of 5.8 dB at 487.5 MHz. First, we convert the gain from decibels to a linear scale: $G = 10^{(5.8/10)} \approx 3.8$. The wavelength at this frequency is $\lambda = c/f \approx 0.615$ m. Using these values, we can calculate the effective area:

$$A_{\rm eff} = \frac{(0.615\ {\rm m})^2 \times 3.8}{4\pi} \approx 0.114\ {\rm m}^2$$

Plugging the final T_{sys} and the newly calculated A_{eff} back into the SEFD equation:

$$\text{SEFD} = \frac{2k_B T_{\text{sys}}}{N_{\text{ant}} A_{\text{eff}}} = \frac{2(1.38 \times 10^{-23}\ \text{J/K})(35\ \text{K})}{(256)(0.114\ \text{m}^2)} \approx 3.3\ \text{kJy}$$

This final predicted sensitivity of 3.3 kJy is substantially better than our initial requirement of 5 kJy, demonstrating that the antenna and LNA system developed in this work successfully meets the stringent performance requirements for the CASM-256 science mission.

Chapter 5

CASM ARRAY IMPLEMENTATION

5.1 Location

The CASM-256 array will be constructed on the site of the DSA-110 array at Owens Valley Radio Observatory (Figure 5.1a). There is already a big “T" shape of concrete there, and the middle portion does not have anything on it, so it will be the perfect place for our array (Figure 5.1b). It also already has power and cable conduit leading back to the correlator room in the basement of the Mayer Building, so we will not need to install new infrastructure.

The proposed layout for the antennas is shown in Figure 5.1c. The two patches in the middle of randomly spaced antennas is an approximation of the trapezoidal portions of concrete extending from the main column of the tee, where we plan to place a few extra antennas to boost east-west angular resolution. Not shown are the planned outrigger stations, which will have about ten antennas each, and will be placed at the far corners of OVRO property for a maximum total baseline of about 2 km. These outrigger stations also have existing infrastructure from DSA-110.

Specifics are lacking because the details have not been finalized. We are still investigating the optimal placement of antennas, which will also depend on the final design of the radomes, which is outside the scope of this thesis.

One of the most significant cost-drivers of the array is low-loss coaxial cable. We need to minimize the length of coax between the antennas and the digital back end. After digitizing, the information can be sent over fiber optic cable, which is significantly cheaper. The solution is to put the back end as close to the array as possible. This will be possible again thanks to existing DSA-110 infrastructure. There is an underground cable vault right next to the tee which has just enough space for a server rack and also pipes for fiber optic cables that run back to the correlator room (Figure 5.2).

5.2 The Back End

The CASM back end consists of two main components: the signal conditioning board, and the analog-to-digital converter (ADC). The former will require a custom solution. For the latter, we will use the Smart Network ADC Processor (SNAP) developed by the CASPER collaboration. It uses an FPGA to collect the data from ADCs, process and channelize it, and send it through network packets to a server for further processing. One SNAP board can sample 12 inputs simultaneously at 250 Mega-samples per second, for a bandwidth of 125 MHz. For CASM, we’re interested in signals in the fourth Nyquist zone, or 375-500 MHz, so the main job of the signal conditioning board is to filter out everything outside of that zone to prevent aliasing.

The full block diagram of the analog signal path is shown in Figure 5.3.

Signal Conditioning Board

The signal conditioning board’s job is threefold:

1. Provide DC bias to the antenna over the coax cable to power the front end amplifier,

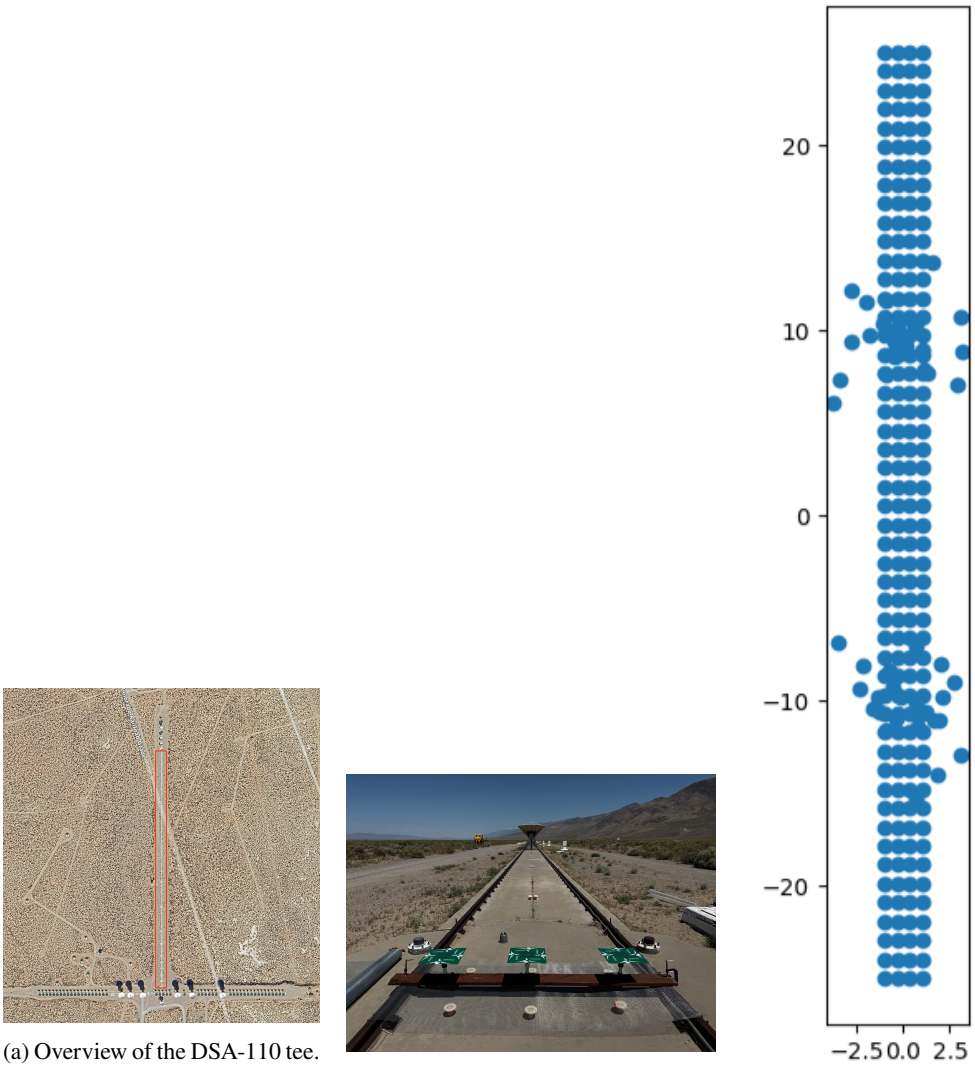

(a) Overview of the DSA-110 tee. Planned location for core array outlined in red.

(b) Test installation at the north end of the tee.

(c) Proposed core array layout.

Figure 5.1: The proposed site for the CASM-256 core array at Owens Valley Radio Observatory.

2. Apply some more gain to make up for the loss from the coax cable, and

3. Anti-alias filter the signal (bandpass from 375-500 MHz) before passing it to the SNAP.

For prototyping and testing purposes, we will split the signal conditioning board's functions into two PCBs — one for DC bias and amplification (Figure 5.4), and the other for the anti-alias filter (Figure 5.5a). Once again, these PCBs were designed for a 1.6 mm thick, four-layer FR-4 stackup. Having four layers instead of two helped with routing power in this relatively small area, and also decreases dielectric loss even further since the copper layers are even closer together than in a two-layer 0.8 mm PCB. A metal cover can be soldered over the components on the top layer, providing robust shielding from RFI. The input and output signals are routed underneath the edges of the cover on the second inner layer between the power and ground planes for even more shielding. The input and

(a) Outside of the cable vault.

(b) Inside the cable vault. Liam Connor shown for scale.

Figure 5.2: Cable vault next to the OVRO tee which will house the CASM-256 back end.

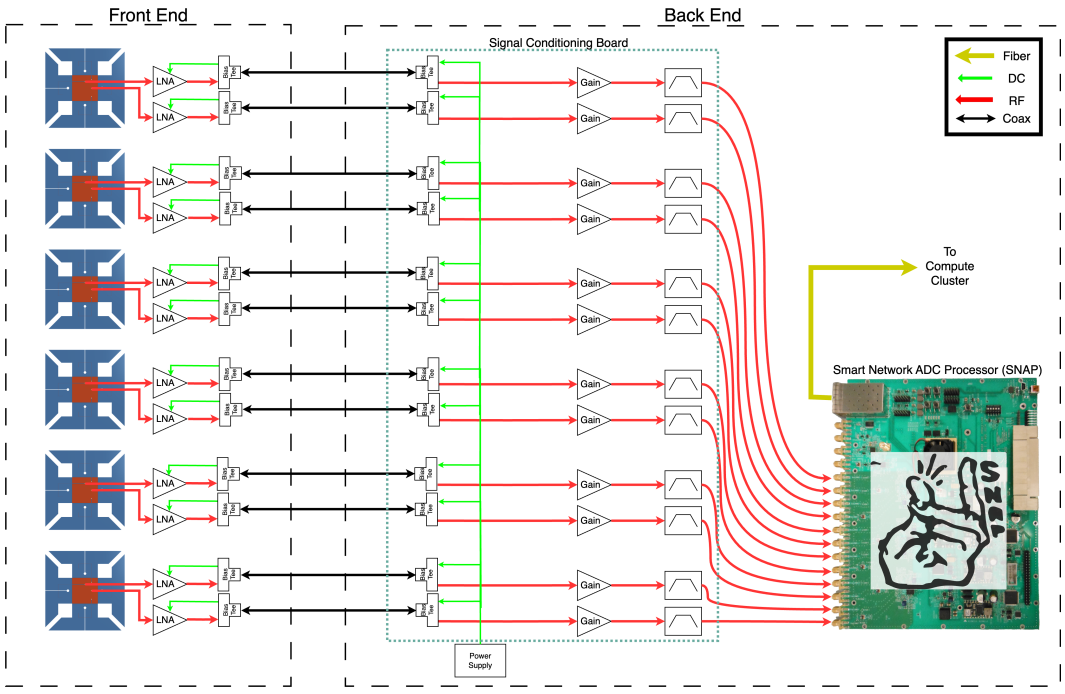

Figure 5.3: Block diagram of full analog signal path for CASM-256 array

output pads are castellated on the edges for surface-mounting onto the antenna PCB, or alternatively are spaced properly for SMA connectors to be soldered on for VNA testing.

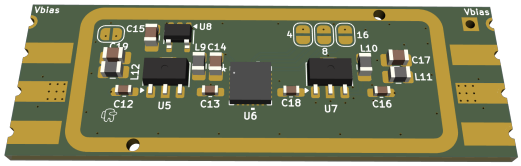

Figure 5.4: Amplification and Bias Tee PCB for the back end signal conditioning board. Uses two MiniCircuits GALI-74+ amplifiers with a F1958NBGK8 variable attenuator in between. There are solder jumpers to configure the attenuation amount because we weren't initially sure how much we would want. There is a voltage regulator which provides 5 V power to the amplifiers. The input power to the voltage regulator is provided by the bias voltage on the output (right side). There are built-in bias tees connecting the DC bias of the input and output center conductors to the Vbias pad on the corresponding side. There is also a solder jumper to connect the DC bias of the input and output. The intended use case for the back end has the output side surface-mounted to a base PCB and an SMA connector soldered to the input side, which would connect to a coax cable going to the antenna. The base PCB would provide the same input voltage to both the back end and front end amplifiers through the bias tees on this PCB. We added the extra flexibility and different ways of powering the input and output bias voltages just in case it became useful. Schematic in Figure B.3.

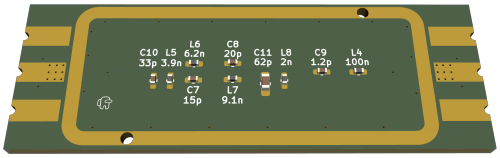

(a) PCB layout of the filter

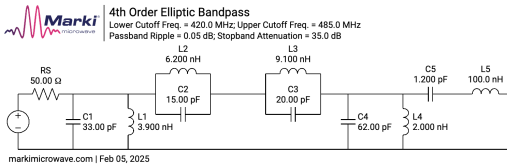

(b) Schematic for filter from Marki Microwave LC Filter Design Tool

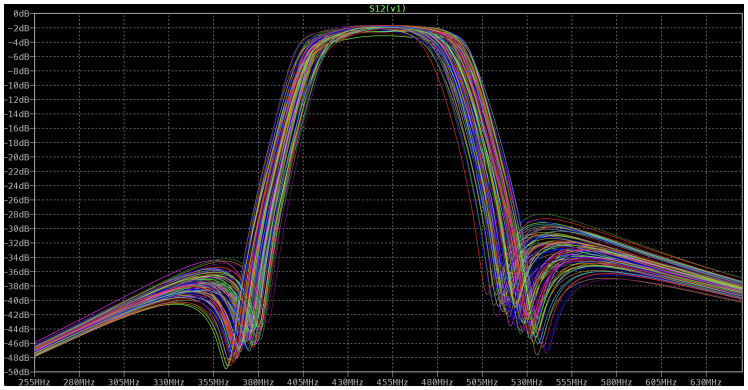

(c) Monte-Carlo simulations of S_{21} in LT Spice with 5% capacitance tolerance and 2% inductor tolerance

Figure 5.5: 4th order elliptic bandpass filter designed for 375-500 MHz.

The base PCB for the amplification and filter PCBs to mount onto has its own 1 A voltage regulator which supplies power for the whole analog signal path for one polarization. These base PCBs stack with nylon standoffs and stacking pin headers for supplying input voltage from a benchtop supply. They stack with an offset of 0.5 inches, which is the separation between input SMA connectors on the SNAP board, allowing the signal conditioning board stack to neatly mate with the SNAP board. See Figure 5.6. Another benefit of the stacking design is the extra layers of copper on the base PCB which provides yet another degree of shielding to prevent crosstalk between adjacent channels.

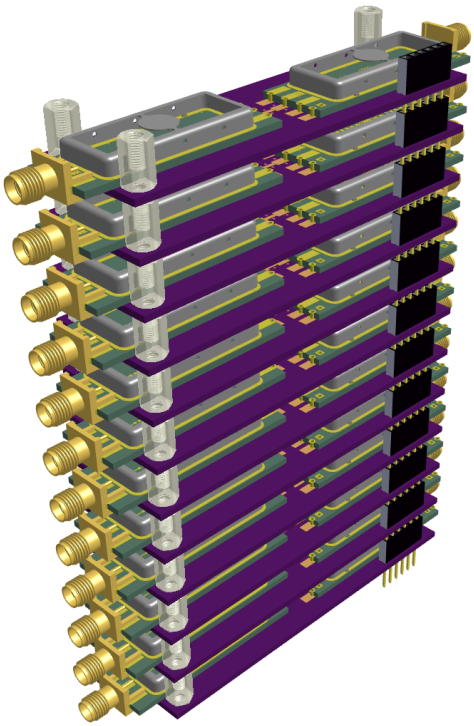

(a) The fully assembled 12-channel signal conditioning board stack.

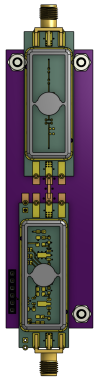

(b) A single channel board, highlighting the modular design.

Figure 5.6: The full back end signal conditioning board

Tests and Lessons Learned

We assembled a few units of the back end board to test, and encountered significant challenges. Basically, nothing worked.

- **The three separate PCBs for the signal conditioning board were a huge pain to assemble.** Surface-mount soldering the separate amplifier and filter PCBs to the base PCB took a lot of extra time, and de-soldering them was way too difficult to make swapping out different test units realistic. We will ditch this strategy in future revisions.
- **Filters need to be simulated extensively with real parasitic component models.** We neglected to do this for the bandpass filter, and its passband in real life ended up being much narrower than desired and also had a minimum insertion loss of -10 dB instead of -2 dB, which is unacceptable. This is probably the main contributor to the unexpected behavior of the signal conditioning board during testing (Figure 5.7).
- **Use a voltage regulator that can supply the current needed.** We used a regulator rated for 200 mA when we needed at least 300 mA for two GALI-74+ amplifiers.
- **Use Design Rules Check tools in PCB layout software.** That would have caught some tiny mistakes in the PCBs we ordered which resulted in the amplifier board being short-circuited

by default, and some pads on the base PCB not being properly grounded. Fixing these by hand was extremely time-consuming.

- **Triple-check the wiring for ICs.** The digital step attenuator between the two GALI-74+ amplifiers on the amplification/bias tee PCB ended up being locked in full 31 dB attenuation mode because the latch enable pin was tied low instead of high. This was impossible to fix by hand so we had to just bypass the attenuator.
- **Don't put DC bias power on the input of a filter which has an inductor shunted to ground.** Obviously (in hindsight) this causes a short-circuit.
- **Again, the amplifier design needs to be done a bit more carefully.** The GALI-74+ chips were also prone to burning out and developing internal shorts on this PCB. This is probably because the bias power on its output pin was provided directly from the regulator through an inductor with no resistor to limit the current.

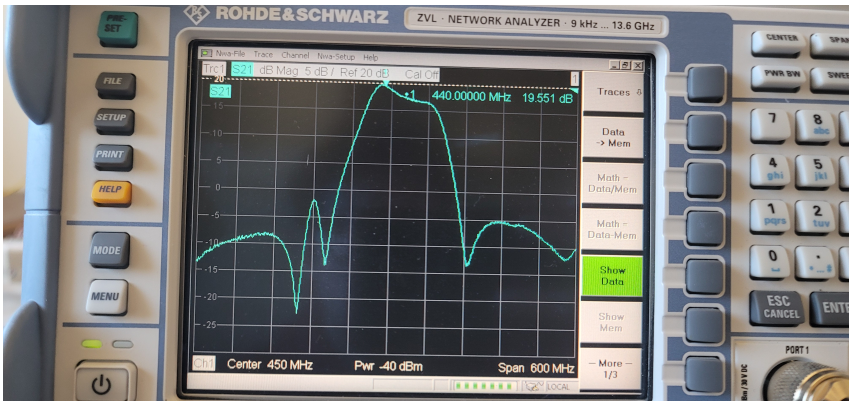

Figure 5.7: VNA readout of a signal conditioning board prototype. The expected gain with the two GALI-74+ amplifiers is about 40 dB in the filter passband, but the prototypes measured only 20 dB.

Chapter 6

DISCUSSION AND NEXT STEPS

We have created promising prototypes and a solid foundation on which to iterate and build the full CASM-256 array. Primarily through the efforts of Liam Connor's group at the Harvard Center for Astrophysics (CfA), we are on track to deploy the array at OVRO by late summer 2025. What follows is an assessment of the remaining work needed on the analog signal path.

The PCB antenna is actually in quite good shape, since it passes the vital benchmarks of FoV and bandwidth, though there is still room to improve. Particularly, the nuances of the matching network still need to be fully understood by simulating the microstrip and slotline components individually. Right now, both of them are open stubs when the original design calls for one of them to be shorted. This definitely needs to be optimized in order to tamp down on undesired resonances which might pop up in array configuration once mutual coupling becomes a possibility.

On that topic, detailed array simulations are also in order. We have not done much of this since we don't have access to sufficient compute power. This is necessary to evaluate the effects of mutual coupling on the antenna S-parameters. It will also be helpful to test out different array configurations, especially including the outrigger antennas, to more specifically inform what is necessary to achieve the CASM-256 science goals.

In terms of mechanical design for the antenna, this is a challenge being actively investigated by the folks at CfA. The main challenge is finding a weatherproof solution which is RF-transparent and cheap enough to scale up. We also want it to be modular, allowing individual rows of antennas to be removed and repaired without disrupting an entire section of the array. The team is currently looking into hollow PVC fenceposts for a base material through which coax cable can be easily routed.

For electronics, the most important un-finalized piece is the LNA. The version presented in this thesis does not work reliably, so our colleague Saren Daghlian at Caltech is working on designing a custom LNA around the MiniCircuits RF transistor SAV-581+. Initial prototypes have achieved a noise temperature of 10 K, which is excellent. The plan is to integrate it with the PCB antenna using low-loss SMA connectors, since this maximizes modularity and ease of handling. It could be optimized further by doing a co-design revision to match the LNA directly to the antenna without necessarily matching both to 50 Ω first, but this would likely be very time-consuming, and since the deployment goal is the end of the summer, the connectorized version should suffice for this first array.

Finally, the back end signal conditioning board needs a complete redesign. The bandpass filter can be tuned and optimized using Cadence Microwave Office or Keysight ADS to account for parasitics of small surface-mount passive components, and that will likely fix the -10 dB return loss issue. The bias tee is not complicated and will work fine if the path from the voltage input on the PCB is routed directly with thick traces. The amplifier will require a bit more thought, but from the initial tests with a working antenna LNA and 100 ft. of coax, it is clear that two GALI-74+ stages are not necessary; just one should be plenty of gain. We should also take care to add a resistor in series with the DC input to the GALI-74+, since the failure to do that seems to have caused several units to burn out.

Overall, we are very satisfied with the state of the analog front end design presented here. The PCB antenna combined with the new SAV-581+ based LNA is both low-cost and low-noise, and should scale nicely to the full 256-array.

Appendix A

DETAILED SIMULATION PARAMETERS

All HFSS simulations were done in Ansys Electronics Desktop 2024 R2 with the Terminal Network solution type using PML boundaries and a Perfect E ground plane sized 2×2 meters. We used the `Auto` solver setup on the default `Balanced` setting with discrete frequency sweeps. The input port for each polarization of the antenna was set to a characteristic impedance of 50 Ω . The benchmark quantities we used were the self-terms of the Terminal S-parameters (i.e. S_{11}, S_{22}) in dB, and the Realized Gain of the antenna from the far fields report, also in dB.

Appendix B

PCB SCHEMATICS

B.1 CASM-6 Front End

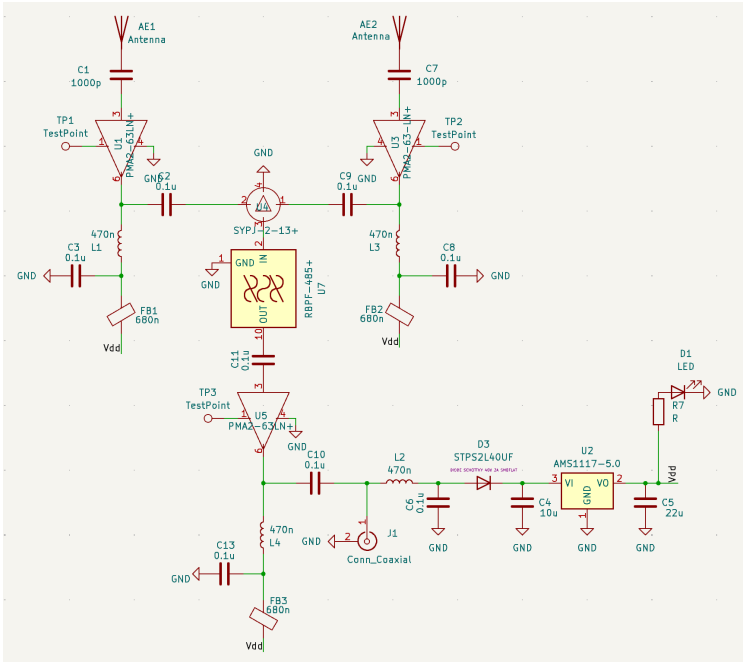

Figure B.1: Schematic for one polarization of the CASM-6 analog front end PCB.

B.2 CASM-256 Front End LNA

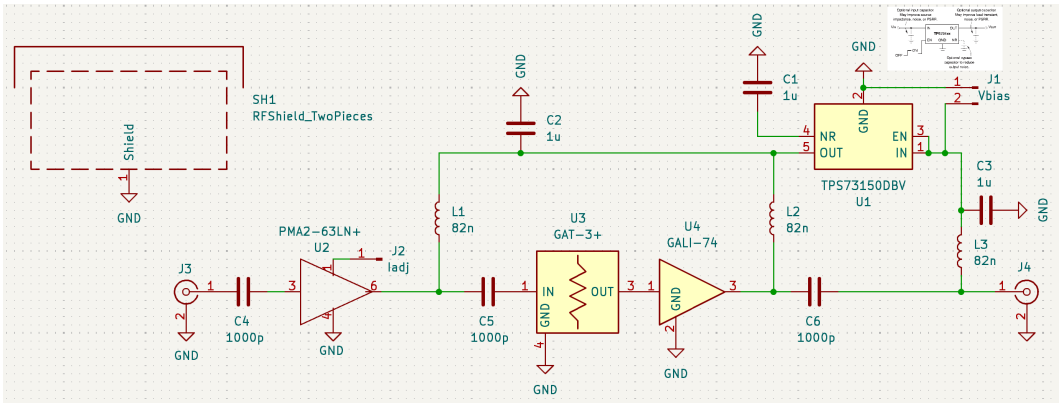

Figure B.2: Schematic for the CASM-256 front end LNA board, featuring two amplification stages and castellated pads for surface-mounting.

B.3 CASM-256 Back End Signal Conditioning Board

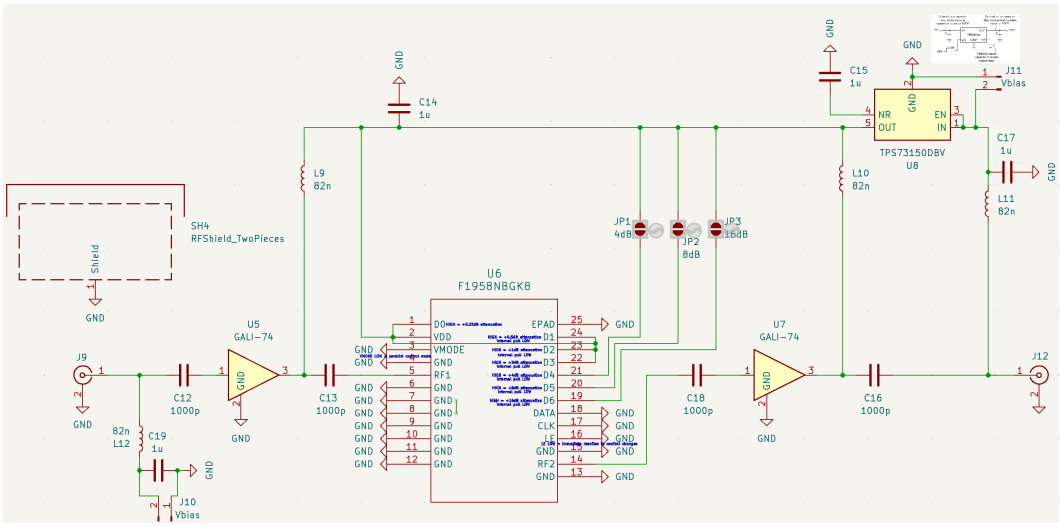

Figure B.3: Schematic for the back end amplifier and bias tee board, designed to provide gain and power over coax to the front end.

Appendix C

ANALYTICAL EQUATIONS FOR THE PRINTED DIPOLE

From Li et al., 2009:

$$Z_{in,slot} = Z_{0,slot} \frac{Z_{dipole} + jZ_{0,slot} \tan \beta_{slot} l_{slot}}{Z_{0,slot} + jZ_{dipole} \tan \beta_{slot} l_{slot}} \tag{C.1}$$

$$Z_{feedpoint} = \frac{jZ_{in,slot} Z_{0,slot} \tan \beta_{slot} l_{short}}{Z_{in,slot} + jZ_{0,slot} \tan \beta_{slot} l_{short}} \tag{C.2}$$

$$Z_{in,feedpoint} = n^2 Z_{feedpoint} \tag{C.3}$$

$$Z_{in,ant} = Z_{in,feedpoint} - jZ_{0,microstrip} \cot \beta_{microstrip} l_{open} \tag{C.4}$$

We can calculate $Z_{0,microstrip}$ and $\beta_{microstrip}$ from ε_r, PCB thickness, and copper width. We can find Z_{dipole} from simulation and work from there to calculate a starting point for the remaining dimensions. Alternatively, we could start with simulating $Z_{feedpoint}$ since parasitics might make the equation for $Z_{in,slot}$ more inaccurate at our lower frequencies (sub-GHz) than used in the paper. Also turns out that nobody has figured out a closed form solution for $Z_{0,slot}$ and β_{slot} (for low ε_r and w_s/λ_c values relevant here), so we're going to have to simulate those, too (Garg, Bahl, and Bozzi, 2013).

Appendix D

DIMENSIONS OF THE PCB ANTENNA

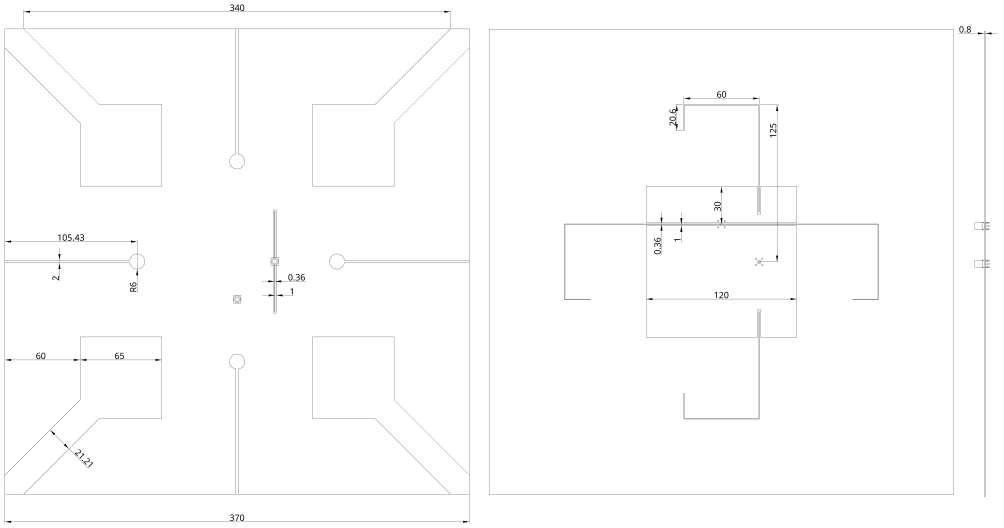

Figure D.1: Copper dimensions of the PCB antenna presented in this thesis

BIBLIOGRAPHY

Bochenek, C. D. et al. (Nov. 2020). "A fast radio burst associated with a Galactic magnetar". In: *Nature* 587.7832, pp. 59–62. ISSN: 14764687. DOI: 10.1038/s41586-020-2872-x.

Collaboration, The CHIME/FRB et al. (June 2021). "The First CHIME/FRB Fast Radio Burst Catalog". In: DOI: 10.3847/1538-4365/ac33ab. URL: http://arxiv.org/abs/2106.04352%20http://dx.doi.org/10.3847/1538-4365/ac33ab.

Connor, Liam et al. (Sept. 2024). "A gas rich cosmic web revealed by partitioning the missing baryons". In: *arXiv*, arXiv:2409.16952. DOI: 10.48550/ARXIV.2409.16952. URL: https://ui.adsabs.harvard.edu/abs/2024arXiv240916952C/abstract.

Deng, Meiling (2012). "The Cloverleaf Antenna: A Compact Wide-bandwidth Dual-polarization Feed for CHIME". PhD thesis. University of British Columbia. DOI: 10.14288/1.0167600. URL: http://hdl.handle.net/2429/50288.

Gallardo, Diego et al. (Jan. 2025). "An Ultra-Wideband Dual Polarization Antenna Array for the Detection and Localization of Bright Fast Radio Transients in the Milky Way". In: *Journal of Astronomical Instrumentation*. URL: http://arxiv.org/abs/2501.08764.

Garg, Ramesh., Inder. Bahl, and Maurizio. Bozzi (2013). "Microstrip Lines and Slotlines". In: p. 603.

Hallinan, G. et al. (July 2019). "The DSA-2000 — A Radio Survey Camera". In: *BAAS* 51.7, p. 255. DOI: 10.48550/ARXIV.1907.07648. URL: https://ui.adsabs.harvard.edu/abs/2019BAAS...51g.255H/abstract.

Hicks, Brian et al. (2009). *Collected LWA Engineering Memos from the Development of the Front End Electronics (FEE)*. Tech. rep. 7. URL: https://leo.phys.unm.edu/~lwa/memos/memo/lwa0190.pdf.

Kuhn, Emily R. et al. (July 2022). "Antenna characterization for the HIRAX experiment". In: URL: https://arxiv.org/pdf/2207.12461.

Li, Rong Lin et al. (2009). "Equivalent-circuit analysis of a broadband printed dipole with adjusted Integrated balun and an array for base station applications". In: *IEEE Transactions on Antennas and Propagation* 57.7, pp. 2180–2184. ISSN: 0018926X. DOI: 10.1109/TAP.2009.2021967.

Most, Elias R. and Alexander A. Philippov (July 2022). "Reconnection-powered fast radio transients from coalescing neutron star binaries". In: *Physical Review Letters* 130.24. DOI: 10.1103/PhysRevLett.130.245201. URL: http://arxiv.org/abs/2207.14435%20http://dx.doi.org/10.1103/PhysRevLett.130.245201.

Newburgh, L. B. et al. (July 2016). "HIRAX: A Probe of Dark Energy and Radio Transients". In: DOI: 10.1117/12.2234286. URL: http://arxiv.org/abs/1607.02059%20http://dx.doi.org/10.1117/12.2234286.

Oliveira-Costa, Angélica de et al. (July 2008). "A model of diffuse Galactic radio emission from 10 MHz to 100 GHz". In: *Monthly Notices of the Royal Astronomical Society* 388.1, pp. 247–260. ISSN: 0035-8711. DOI: 10.1111/J.1365-2966.2008.13376.X. URL: https://dx.doi.org/10.1111/j.1365-2966.2008.13376.x.

Oppermann, Niels, Liam Connor, and Ue-Li Pen (Apr. 2016). "The Euclidean distribution of Fast Radio Bursts". In: *Monthly Notices of the Royal Astronomical Society* 461.1, pp. 984–987. DOI: 10.1093/mnras/stw1401. URL: http://arxiv.org/abs/1604.03909%20http://dx.doi.org/10.1093/mnras/stw1401.

Ravi, Vikram et al. (May 2023). "Deep Synoptic Array Science: Discovery of the Host Galaxy of FRB 20220912A". In: *The Astrophysical Journal Letters* 949.1, p. L3. ISSN: 2041-8205. DOI: 10.3847/2041-8213/acc4b6. URL: https://iopscience.iop.org/article/10.3847/2041-8213/acc4b6.

Sharma, Kritti (2024). "Deep Synoptic Array-110 Catalog of Fast Radio Bursts and their Host Galaxies". In: *AAS* 243, p. 319.03. URL: https://ui.adsabs.harvard.edu/abs/2024AAS...24331903S/abstract.

Sun, Hai Han et al. (Dec. 2018). "Wideband Planarized Dual-Linearly-Polarized Dipole Antenna and Its Integration for Dual-Circularly-Polarized Radiation". In: *IEEE Antennas and Wireless Propagation Letters* 17.12, pp. 2289–2293. ISSN: 15361225. DOI: 10.1109/LAWP.2018.2873117.